1 **Geochronological and Geochemical Effects of Zircon Chemical Abrasion: Insights from Single-**
2 **Crystal Stepwise Dissolution Experiments**

4 **Alyssa J. McKanna[1], Blair Schoene[1], and Dawid Szymanowski[1,2]**
5
6 [1]Princeton University, Department of Geosciences, Princeton, New Jersey 08544, USA
7 [2]Institute of Geochemistry and Petrology, ETH Zurich, 8092 Zurich, Switzerland
8
9 **Correspondence:** Alyssa J. McKanna (ajmckanna@gmail.com)

10 **Abstract**

11 Chemical abrasion in hydrofluoric acid (HF) is routinely applied to zircon grains prior to U-Pb
12 dating by isotope dilution thermal ionization mass spectrometry (ID-TIMS) to remove radiation-
13 damaged portions of grains affected by Pb loss. Still, many chemically abraded datasets exhibit
14 evidence of residual Pb loss. Here we test how the temperature and duration of chemical
15 abrasion affects zircon U-Pb and trace element systematics in a series of 4-hour, single-crystal
16 stepwise dissolution experiments at 180 °C and 210 °C. Microtextural data for the zircon
17 samples studied is presented in a complementary paper by McKanna et al. (2023). We find that
18 stepwise dissolution at 210 °C is more effective at eliminating U, common Pb (Pb_c), and light
19 rare earth element (LREE) enriched material affected by open system behavior; reduces the
20 presence of leaching-induced artefacts that manifest as reverse discordance; and produces
21 more consistent and concordant results in zircon from the three rocks studied. We estimate
22 that stepwise dissolution in three 4 h steps is roughly equivalent to a single ~8 h leaching step
23 due to the insulating properties of the PTFE sleeve in the Parr pressure dissolution vessel,
24 whereas traditionally labs utilize a single 12-hour leaching step. We conclude that a single 8 h
25 leaching step at 210 °C should remove Pb loss effects in the majority of zircon and that this can
26 be used as an effective approach for routine analysis. Further, we calculate time-integrated
27 alpha doses for leachates and residues from measured radionuclide concentrations to
28 investigate: 1) the alpha dose of the material dissolved at the two leaching conditions, and 2)
29 the apparent minimum alpha dose required for Pb loss susceptibility: $\geq 6 \times 10^{17}$ α/g.

31 **1. Introduction**

32 Zircon U-Pb geochronology by isotope dilution thermal ionization mass spectrometry (ID-TIMS)
33 has played a pivotal role in constraining the timing and tempo of processes on Earth from the
34 Hadean to the Pleistocene. Zircon is a remarkable chronometer, in part because crystalline
35 zircon is exceptionally chemically and physically durable. The zircon structure, however, can
36 accumulate radiation damage over time. Radiation damage is principally caused by alpha recoil
37 events in the ^{238}U, ^{235}U, and ^{232}Th decay series and the spontaneous fission of ^{238}U (Ewing et al.,
38 2003; Meldrum et al., 1998; Weber, 1990). Radiation-damaged zircon can lose Pb and less
39 commonly U, violating the basic requirement of geochronology that neither parent nor
40 daughter isotopes are lost through time except through radioactive decay (Geisler et al., 2002).
41 Fortunately, the dual $^{206}Pb/^{238}U$ and $^{207}Pb/^{235}U$ decay schemes provide a self-check mechanism

42   by which open system behavior can be identified in zircons older than several hundred Ma
43   (Mezger and Krogstad, 1997; Corfu, 2013). In the Phanerozoic, however, the dual decay system
44   becomes less effective at recognizing Pb-loss, since the trajectory of Pb-loss follows concordia,
45   and the precision of ^{207}Pb/^{235}U dates is also lower than corresponding ^{206}Pb/^{238}U dates due to
46   the lower isotopic abundance of ^{235}U and consequently ^{207}Pb (Corfu, 2013; Schoene, 2014).

47   In a seminal study, Mattinson (2005, 2011) – building off the previous findings of Krogh and
48   Davis (1975) and Todt and Büsch (1981) – demonstrated that the most radiation-damaged
49   portions of zircon can be effectively removed by hydrofluoric acid (HF) through a series of
50   stepwise dissolution experiments on multi-grain aliquots. He showed that early leaching steps
51   sampled high-U material with discordant U-Pb dates, while later leaching steps sampled low-U
52   residues unaffected by open-system behavior. Mattinson (2005, 2011) further established that
53   partially annealing zircon samples prior to leaching helps to minimize the unwanted elemental
54   and isotopic fractionation effects that plagued earlier leaching attempts (Davis & Krogh, 2000;
55   Todt & Büsch, 1981). These experimental findings revolutionized the field of zircon U-Pb
56   geochronology by allowing scientists to attain meaningful geochronological results from
57   previously unusable zircon affected by open-system behavior. Air abrasion – the pre-treatment
58   technique previously used to improve U-Pb concordance by removing crystal rims which tend
59   to be more exposed to alteration (Krogh, 1981) – was largely abandoned. Today, a variation of
60   Mattison's approach – termed chemical abrasion – is applied to virtually all zircon grains prior
61   to ID-TIMS U-Pb isotopic analysis. In this variation, zircon crystals are annealed at 800 °C to
62   1200 °C for 36 h to 60 h and then leached in concentrated HF at 180 °C to 210 °C for 10 h to 18
63   h prior to dissolution and isotopic analysis (Mundil et al., 2004; Huyskens et al., 2016; Widmann
64   et al., 2019).

65   The decrease in sample size from multi-grain aliquots to portions of single crystals and the
66   concurrent increase in analytical precision in TIMS over the past half-century (e.g., Schoene,
67   2014) demands a critical re-evaluation of the chemical abrasion technique and the accuracy of
68   the U-Pb ages that the Earth science community has come to rely on. Many studies have now
69   shown that chemically abraded zircon samples often still exhibit residual Pb-loss. This challenge
70   is widely recognized in the ID-TIMS U-Pb community and has prompted investigations into the
71   effects of different annealing and leaching conditions on geochronological outcomes (Huyskens
72   et al., 2016; Widmann et al., 2019), new statistical approaches for evaluating over-dispersed U-
73   Pb datasets (Keller, 2023), and microstructural studies of chemically abraded zircon (McKanna
74   et al., 2023).

75   We build on the earlier work of Mattinson (2005, 2011) and present a series of new stepwise
76   dissolution experiments performed at the single-crystal scale. We evaluate the effects of
77   stepwise chemical abrasion at 180 °C and 210 °C on zircon U-Pb and trace element systematics
78   in three zircon samples – AS3, SAM-47, and KR18-04 – which span a range of crystallization
79   ages, geological settings, and radiation damage densities. These zircons come from the same
80   sample aliquots as studied by McKanna et al. (2023) in their recent microstructural
81   investigation of zircon dissolution which presents a unique opportunity to integrate zircon
82   microtextures, geochronology, and geochemistry.

2. Methods

Zircon samples were annealed in quartz crucibles at 900 °C for 48 h in air in a box furnace prior to the start of the experiments. Annealed grains were mounted in epoxy, polished, and imaged by cathodoluminescence (CL) or backscattered electron (BSE) imaging using a XL30 FEG scanning electron microscope equipped with a mini-Gatan CL detector and a semiconductor BSE detector housed at the PRISM Imaging and Analysis Center at Princeton University. Images of dated zircon crystals are presented in Fig. S1, Fig. S2, and Fig. S3.

The stepwise partial dissolution protocol outlined here is very similar to that of Keller et al., (2019, their Fig. 1). Crystals were plucked from their epoxy mounts, rinsed in 30% HNO_3, and individually transferred to 200 µL PFA microcapsules for partial dissolution in ~100 µL of concentrated HF. Microcapsules were loaded into a PTFE-lined Parr pressure dissolution vessel with 5 mL moat HF and placed in a box oven set to 180 °C or 210 °C for a period of 4 h. At the 4 h mark, the pressure vessel was removed from the oven and placed in front of a fan to cool to room temperature.

The microcapsules were then removed from the pressure vessel and the leachate (the dissolved zircon-HF mixture) from each microcapsule was transferred to a clean 7 mL PFA beaker using a pipette. A fresh, acid-cleaned pipette tip was used for each sample transfer. Approximately 100 µL of 6N HCl was added to the residue (the remaining undissolved zircon) in the microcapsule, and the microcapsule was capped and placed on the hotplate for 1 h. The 6N HCl was then pipetted off the residue and added to the 7 mL PFA beaker with the sample leachate. The residue was then sequentially rinsed in the microcapsule using a pipette with 3N HCl, 6N HCl, 30 % HNO_3, and concentrated HF. These rinses were discarded. About 100 µL of fresh concentrated HF was then added to each residue for the second round of step leaching. In total, samples were partially dissolved in a series of three 4-h leaching steps generating a L1, L2, and L3 leachate for each zircon crystal.

After the L3 leachate was collected, the residue was again rinsed with acid and ~100 µL of fresh HF was added to the microcapsule. Each residue was spiked with the EARTHTIME [205]Pb-[233]U-[235]U tracer (Condon et al., 2015; McLean et al., 2015) and dissolved in a Parr pressure dissolution vessel in a box oven at 210 °C for 48 to 60 h. Each leachate was spiked with the same tracer, capped, and placed on the hot plate for the same duration. Both leachates and residues were then dried down on the hot plate. Residues were redissolved in ~100 µL of 6N HCl in the Parr pressure vessel in the box oven at 180 °C overnight, and leachates were redissolved in ~100 µL of 6N HCl on an 80 °C hot plate overnight. Afterward, all residues and leachates were dried down on the hot plate and redissolved in 3N HCl in preparation for ion exchange chromatography. This procedure was modified slightly for half of the KR18-04 zircon samples treated at 210 °C to evaluate whether the incomplete dissolution of fluoride salts was causing unwanted U-Pb elemental fractionation effects. For these samples, after each HF leachate was collected, zircon residues were dried down completely on the hot plate before the addition of ~100 µL of 6N HCl. Microcaps were then transferred back to the Parr pressure vessel and redissolved at 180 °C overnight in the box oven. The 6N HCl liquid was then pipetted off the

127 residue and added to the sample's HF leachate in the 7 mL PFA beaker. This procedure was
128 repeated for the L2 and L3 leachates. All other steps remained the same.
129
130 PTFE columns were prepared with 50 μL of Eichrom AG1-X8 anion exchange resin, cleaned, and
131 equilibrated. U-Pb ion exchange chemistry followed the protocol established by Krogh (1973)
132 and modified by Schoene et al. (2010) for the collection of trace elements. Combined U and Pb
133 fractions were dried down with trace 0.05 M H_3PO_4 and loaded onto a zone-refined Re filament
134 with a Si-gel emitter (Gerstenberger and Haase, 1997) for isotopic analysis on one of the two
135 IsotopX Phoenix TIMS at Princeton University. Pb isotopes were measured on either the
136 Daly/photomultiplier detector or ATONA Faraday system (Szymanowski and Schoene, 2020),
137 and U isotopes were measured as oxides on Faraday cups with 10^{12} Ω resistors or on the
138 ATONA Faraday system. Mass fractionation of Pb isotopic analyses was corrected for with
139 factors specific to each detector system, derived from a compilation of in-run values measured
140 in samples spiked with the EARTHTIME ^{202}Pb-^{205}Pb-^{233}U-^{235}U tracer using the known ^{202}Pb/^{205}Pb
141 ratio of the tracer. Mass fractionation of U isotopic analyses was corrected using the known
142 ^{233}U/^{235}U ratio of the tracer. Tripoli and ET-Redux software (Bowring et al., 2011; McLean et al.,
143 2011) were used for processing isotopic data and error propagation, assuming a sample
144 ^{238}U/^{235}U ratio of 137.818 ± 0.045 (2σ) (Heiss et al., 2012). All reported ^{206}Pb /^{238}U and
145 ^{207}Pb/^{206}Pb dates are calculated using the decay constants of Jaffey et al., (1971) and Th-
146 corrected assuming a magma Th/U ratio of 3.5. Reported uncertainties reflect 2σ analytical
147 uncertainties. Common Pb corrections assume a composition equivalent to the blank.
148
149 Major and trace element analyses were made using a Thermo Scientific iCap-Q inductively
150 coupled plasma mass spectrometer (ICPMS) at Princeton University following the procedure
151 developed by Schoene et al. (2010), with analytical parameters described in O'Connor et al.
152 (2022). U concentrations were calculated from Th concentrations measured by ICPMS and the
153 Th/U ratio estimated from radiogenic ^{208}Pb and the ^{206}Pb/^{238}U age assuming concordance
154 between the U-Pb and Th-Pb systems.
155
156 **3. Geologic setting, sample description, and previous geochronology**
157
158 **3.1. AS3**
159
160 AS3 zircons are from an anorthosite from the Duluth Complex of northern Minnesota, USA
161 which formed during the Mesoproterozoic North American Midcontinent Rift (46°45'43.4" N,
162 92°09'32.4" W) (Paces & Miller, 1993; Miller et al., 2002; Schmitz et al., 2003; Swanson-Hysell
163 et al., 2019, 2020). The Duluth Complex is a massive layered mafic intrusion. The anorthositic
164 and layered series of the complex were emplaced at ~1096 Ma over a duration <1 m.y.
165 (Swanson-Hysell et al., 2020). The voluminous magmatism that formed the Duluth Complex is
166 attributed to decompression melting due to lithospheric extension occurring atop an upwelling
167 mantle plume (Swanson-Hysell et al., 2020). Rifting in the region ceased at ~1084 Ma (Swanson-
168 Hysell et al., 2019). Thermochronology data from the Minnesota River Valley in southern
169 Minnesota suggest that rocks in the region have sat at near-surface temperature conditions
170 since the Neoproterozoic (Guenthner et al., 2013; McDannell et al., 2022).

171

172   The AS3 sample studied is the same as that of Takehara et al. (2018). The rock sample is

173   composed of plagioclase, amphibole, clinopyroxene, and ilmenite with minor K-feldspar,

174   apatite, zircon, and baddeleyite. Partially chloritized amphiboles, altered plagioclase, and

175   zeolite veins indicate that this sample of AS3 has interacted with low-temperature

176   hydrothermal fluids as previously described (Takehara et al., 2018). Zircon grains are large and

177   occur as orange-to-orangish brown tabular prisms or anhedral shards. Grains are fractured and

178   often have large melt inclusions elongated parallel to the *c*-axis. Crystals exhibit concentric and

179   convolute zonation patterns, and many grains are hydrothermally altered (Fig. S1) (McKanna et

180   al., 2023; Takehara et al., 2018). Altered grains and grains with inclusions were included in the

181   experiments to evaluate how well geochemical data traces the dissolution of inclusions and

182   altered material. Raman data indicate that grains have accumulated high radiation damage

183   densities with equivalent alpha doses of 2×10^{17} to $>1\times10^{19}$ α/g with significant intracrystalline

184   variations in radiation damage (McKanna et al., 2023).

185

186   Paces and Miller (1993) presented the first U-Pb geochronological data for AS3 zircon. These

187   authors found that six multi-grain aliquots of air-abraded zircon crystals produced concordant

188   ID-TIMS U-Pb dates and assigned the sample a weighted-mean $^{207}Pb/^{206}Pb$ age of 1099.1 ± 0.5

189   Ma (2σ). Schmitz et al. (2003) later conducted additional ID-TIMS U-Pb isotopic analysis on

190   individual air-abraded AS3 zircon. The authors found that several crystals produced discordant

191   dates affected by recent Pb loss. Twelve concordant analyses yielded a concordia age of 1099.1

192   ± 0.2 Ma (2σ). Eight grains from the same sample were later analyzed by chemical abrasion ID-

193   TIMS by Schoene et al. (2006). The authors annealed grains at 900 °C for 60 h and chemically

194   abraded them in an HF-HNO$_3$ mixture at 180 °C for 12 to 14 h. Residues produced concordant

195   dates with weighted mean $^{206}Pb/^{238}U$ and $^{207}Pb/^{206}Pb$ ages of 1095.9 ± 0.2 Ma and 1098.6 ± 0.3

196   (2σ) assuming a zircon $^{238}U/^{235}U$ ratio of 137.88. Recalculating from published isotope ratios

197   (Schoene et al., 2006) and assuming an updated zircon $^{238}U/^{235}U$ of 137.818 ± 0.045 (2σ) (Heiss

198   et al., 2012) in the age equation yields a $^{207}Pb/^{206}Pb$ age of 1097.7 ± 0.3 (2σ). Age differences

199   between these and previous results were attributed by the authors to differences in tracer

200   calibration, which had been redone as part of Schoene et al. (2006). Takehara et al., (2018) later

201   demonstrated that zircons from a different sample of AS3 collected from the same sample

202   locality are strongly affected by alteration; sensitive high-resolution ion microprobe (SHRIMP)

203   analyses showed that altered zones yielded normally discordant U-Pb analyses; were enriched

204   in incompatible trace elements including LREEs, Ca, Mn, Fe, Al, Li, and K; and depleted in Zr and

205   Si.

206   **3.2 SAM-47**

207   SAM-47 is an Archean (~3.32 - 3.29 Ga) granodiorite from the Corunna Downs Granitic Complex

208   of the Emu Pools Supersuite in the eastern Pilbara Craton (21°24'29.01" S, 119°46'21.03" E)

209   (Barley and Pickard, 1999; Smithies et al., 2003; Van Kranendonk et al., 2007). The tectonic

210   significance of the dome and keel structures of the eastern Pilbara Craton are a matter of

211   debate (stagnate lid versus mobile lid tectonics), and the region has experienced a multi-phase

212   deformational history (Kloppenburg et al., 2001; MacLennan, 2019; Moore and Webb, 2013).

213 ID-TIMS U-Pb ages for apatite from the Corunna Downs Granitic Complex are ~3.3 Ga which are
214 similar to Ar-Ar ages reported by Kloppenburg (2003). The similarity between the U-Pb and Ar-
215 Ar data suggest rapid cooling through ~460°C following intrusion of the granitoid (MacLennan,
216 2019). Zircon (U-Th)/He dates for the Owen's Gully diorite from the Mount Edgar Granitic
217 Complex north of the Corunna Downs range from 677.5 ± 36.3 to 815.5 ± 44.6 Ma, suggesting
218 that the eastern craton reached near-surface thermal conditions, where radiation damage can
219 accumulate in zircon, sometime in the Neoproterozoic (Magee et al., 2017). Low-temperature
220 thermochronology data from elsewhere in the Pilbara craton (the northern, central, and
221 western blocks) suggest that the onset of widespread cooling related to basin-development and
222 unroofing varied regionally starting sometime between ~600 and 300 Ma (Morón et al., 2020).
223 Zircon grains separated from SAM-47 are euhedral, brown, translucent, and finely-fractured
224 (Fig. S2). Crystals display fine-scale concentric growth zones, and rims are enriched in actinides
225 and radiation damage relative to cores (McKanna et al., 2023). Raman data suggest that grains
226 have accumulated intermediate-to-high radiation damage densities with equivalent alpha doses
227 ranging from 6×10^{17} to 2×10^{18} α/g (McKanna et al., 2023). There is no previous zircon U-Pb
228 geochronology from this sample, however, Pb-loss is common in similarly aged zircon from the
229 Pilbara craton (MacLennan, 2019).

230 **3.3 KR18-04**
231
232 KR18-04 zircons come from a Neoproterozoic rhyolite body associated with the glaciolacustrine
233 Konnarock Formation in the Blue Ridge Mountains of Virginia, USA (MacLennan et al., 2020)
234 (36°41'47.95" N, 81°24'22.08" W). The Konnarock Formation is part of a structurally continuous
235 sedimentary sequence deposited in a continental rift environment (Merschat et al., 2014). This
236 sequence unconformably overlies gneisses that are related to the Mesoproterozoic Grenville
237 orogeny. ID-TIMS U-Pb ages for zircon separated from KR18-04 were used to show that glacial
238 sedimentation was occurring at tropical latitudes at ~751 Ma, 30 million years prior to the
239 Sturtian Snowball Earth (MacLennan et al., 2020). The post-depositional history of the region is
240 complex and poorly resolved (Roden, 1991). Zircon fission track dates (T_c = ~205°C) from the
241 Blue Ridge are variably reset by burial reheating and range in age from ~617 Ma to late
242 Paleozoic dates (Naeser et al., 2016). Zircon (U-Th)/He dates (T_c = ~180 °C for crystalline zircon)
243 from the Blue Ridge are contemporaneous with the late-stages of the Alleghenian orogeny
244 indicating that the zircon He chronometer was fully reset by burial reheating and records
245 synorogenic exhumation (Basler et al., 2021).
246
247 The KR18-04 rhyolite is crystal-rich with prominent, dominantly euhedral K-feldspar and quartz
248 phenocrysts (MacLennan et al., 2020). Zircon grains separated from KR18-04 are euhedral, pink-
249 orange, transparent, and have few to no inclusions. Grains exhibit concentric zoning in
250 cathodoluminescence images with some faint, broad growth zones Click or tap here to enter
251 text.(Fig. S3). Raman data suggest that grains have accumulated low-to-intermediate radiation
252 damage densities with equivalent alpha doses ranging from 5×10^{16} to 2×10^{17} α/g (McKanna et
253 al., 2023).
254

255 Twelve single-crystal zircon ID-TIMS U-Pb analyses for KR18-04 are presented by MacLennan et
256 al. (2020). Zircon were initially chemically abraded at 185 °C for 12 h. However, since many of
257 these analyses retained significant Pb-loss, the intensity of chemical abrasion was increased to
258 210 °C for up to 14 h for the remaining samples. The twelve reported $^{206}Pb/^{238}U$ dates – which
259 combine both leaching conditions – range from 753.08 ± 0.33 to 741.21 ± 0.35 Ma. The
260 reported data are statistically over-dispersed for a single population. The authors attribute the
261 spread in ages along concordia and the one discordant analysis to residual Pb-loss (their Fig.
262 S10). The reported eruption age for the sample derived from the eight oldest analyses and
263 determined using a Bayesian Markov Chain Monte Carlo technique is 752.60 +0.12/-0.65 Ma.
264
265 **4. Results**
266
267 **4.1 U-Pb geochronology**
268
269 **4.1.1 AS3**
270
271 L1 leachates are strongly affected by Pb-loss, and are enriched in Pb_c derived from inclusions
272 and altered zones (Fig. 1, Table S1). L1 leachates either overlap the concordia curve due to large
273 uncertainties or are normally discordant. L2 and L3 leachates are older than L1 leachates and
274 form a discordia line of analyses that are either normally discordant, concordant, or reversely
275 discordant. The lower intercept ages of the discordia lines are zero-age. L2 and L3 leachates
276 treated at 180 °C are more enriched in Pb_c and ages are more widely dispersed compared to L2
277 and L3 leachates treated at 210 °C.
278
279 Residues treated at 210 °C form a single, concordant age population with a weighted mean
280 $^{206}Pb/^{238}U$ age of 1096.42 ± 0.49 Ma (MSWD = 1.7; Fig. 1). U-Pb ages of residues treated at 180
281 °C are dispersed along concordia and include reversely discordant analyses, although a cluster
282 of residue analyses yield a weighted mean $^{206}Pb/^{238}U$ age of 1096.29 ± 0.36 Ma (MSWD = 2.3) in
283 agreement with the 210 °C result. Weighted-mean $^{207}Pb/^{206}Pb$ ages for all leachates and
284 residues agree within uncertainty (Fig. 2). The weighted-mean $^{207}Pb/^{206}Pb$ ages obtained for
285 residues are 1097.03 ± 0.63 Ma (MSWD = 1.7) and 1096.64 ± 0.96 Ma (MSWD = 0.48), for the
286 180°C and 210 °C datasets respectively. The new data agree well with previous geochronology
287 (Schoene et al., 2006).
288
289 **4.1.2 SAM-47**
290
291 L1 leachates from both sample sets are strongly affected by Pb-loss (Fig. 3, Table S1). L2 and L3
292 leachates from the 180 °C experiment are also affected by significant Pb-loss. In contrast, many
293 of the L2 and L3 leachates from the 210 °C experiment are concordant, and the few normally
294 discordant analyses closely approach concordia.
295
296 Residues from the 180 °C dataset form a discordia line with two concordant and four normally
297 discordant analyses. The two concordant residues have a weighted-mean $^{206}Pb/^{238}U$ age of
298 3319.5 ± 1.4 Ma (MSWD = 1.7). All 210 °C residues overlap or closely hug concordia; three

299   concordant residues yield a weighted-mean $^{206}Pb/^{238}U$ age of 3316.1 ± 1.6 Ma (MSWD = 1.0).
300   Upper intercept ages for residues and 210 °C L2 and L3 leachates agree within uncertainty and
301   produce robust MSWDs (Fig. 3). The most precise upper and lower intercept ages are 3321.23
302   +0.78/-0.71 Ma and 751 ± 140 Ma, respectively. Most $^{207}Pb/^{206}Pb$ dates for L2, L3, and residue
303   samples from the 210 °C experiment agree within uncertainty (Fig. 2). 210 °C residues yield a
304   weighted-mean $^{207}Pb/^{206}Pb$ age of 3321.75 ± 0.63 Ma (MSWD = 0.83) in agreement with upper
305   intercept ages. In contrast, $^{207}Pb/^{206}Pb$ dates from the 180 °C dataset are notably younger,
306   indicating the dissolution of domains affected by ancient Pb-loss. The two concordant 180 °C
307   residue analyses yield a weighted-mean $^{207}Pb/^{206}Pb$ age of 3320.90 ± 0.87 (MSWD = 0.050).
308
309   **4.1.3 KR18-04**
310
311   L1 leachates from both sample sets are affected by Pb-loss that occurred at zero-age (Fig. 4,
312   Table S1). L2 leachates from both experiments are concordant and older than zircon residues.
313   L3 leachates are generally concordant, younger than L2 leachates, and slightly older or within
314   uncertainty of zircon residues. Residues from the 180 °C experiment spread along concordia
315   from 758.63 to 752.99 Ma. In contrast, residues from the 210 °C experiment form a tight cluster
316   with a weighted mean $^{206}Pb/^{238}U$ age of 752.49 ± 0.24 Ma (MSWD = 1.1, n=6) in agreement with
317   previous geochronology (MacLennan et al., 2020). This weighted-mean age includes analyses
318   measured on the ATONA which produced more precise U measurements; the batch of samples
319   ran using the traditional amplifiers had very poor U ionization resulting in low quality U
320   measurements. The two 210 °C zircon aliquots that followed slightly different step-leaching
321   protocols as outlined in Methods generated equivalent results.
322
323   **4.2 Trace element geochemistry**
324
325   Major and trace element geochemistry data for AS3, SAM-47, and KR18-04 are reported in
326   Table S2. In the 180 °C experiments, leachates for the three zircon samples are enriched in LREE
327   and Pb_c relative to zircon residues (Fig. 5, Fig. 6, and Fig. 7). LREE enrichment is apparent both
328   in chondrite-normalized REE spider diagrams (Fig. S4, Fig. S5, and Fig. S6) and in LREE-indices
329   (LREE-I) (Table S3). LREE-indices – calculated as [Dy]/[Nd] + [Dy]/[Sm] following Bell et al.,
330   (2016) – quantify LREE-enrichment in zircon which can reflect chemical alteration or sample
331   contamination. The lower the LREE-I, the higher the LREE-enrichment. In the 210 °C
332   experiments, L1 and some L2 leachates are enriched in LREE and Pb_c, but some L2 and all L3
333   leachates have LREE and $Pb*/Pb_c$ compositions similar to residues. Samples' LREE-I and
334   radiogenic to common Pb ratios ($Pb*/Pb_c$) are positively correlated.
335
336   AS3 leachates are enriched in U relative to residues in the 180 °C dataset (Fig. 8 and Table S3),
337   whereas in the 210 °C dataset only L1 leachates are U-enriched. A similar pattern is seen for
338   KR18-04: L1 and L2 leachates from the 180 °C dataset are enriched in U relative to residues, but
339   only L1 leachates are U-enriched in the 210 °C dataset. Results for SAM-47 differ. Some SAM-47
340   leachates are marginally enriched in U in the 180 °C dataset, while most leachates from the 210
341   °C experiment have U compositions similar to residues.
342

343   The percent zircon dissolved is calculated from measured Zr abundances: (Zr_{step}/Zr_{total}) $\times$ 100
344   (Fig. 8 and Table S3). This calculation assumes that zircon residues fully dissolve during the final
345   digestion step. For AS3 samples, most dissolution occurred in L1 with progressively smaller
346   fractions dissolved in L2 and L3. The median fraction of the AS3 residue remaining in the 180 °C
347   and 210 °C experiments is ~55 % and ~30 %, respectively. For SAM-47 samples, only 10 to 20 %
348   of the zircon dissolved during leaching at 180 °C, leaving 80 to 90 % of the zircon available for
349   final digestion. At 210 °C, most dissolution in SAM-47 samples occurred in L1 with progressively
350   smaller volumes dissolved in L2 and L3; zircon residues fractions are less than 40 %. For KR18-
351   04 samples, only ~10 to 15 % of zircon dissolved during leaching at 180 °C, leaving residue
352   fractions of ~85 to 95 %. At 210 °C, ~10 °C to 30 % of KR18-04 zircon dissolved during leaching,
353   resulting in 70 to 90 % residue fractions. Percent Pb* ($Pb*_{step}$/$Pb*_{total}$ $\times$ 100) calculations mirror
354   results for percent zircon dissolved in all experiments (Fig. 8 and Table S3).
355
356   **5. Discussion**
357
358   **5.1 Reverse discordance**
359
360   Reverse discordance and concordant analyses that are older than the samples' interpreted
361   crystallization ages are common in the AS3 and KR18-04 datasets but absent in SAM-47.
362   Concordant analyses that are "too old" can result from either minor U loss or Pb* gain, causing
363   datasets to lie along a discordia line that overlies the concordia curve; for brevity, we will also
364   refer to these analyses as "reversely discordant." Reverse discordance is most common in L2
365   and L3 leachates, however, a subset of residues from the AS3 and KR18-04 180 °C datasets are
366   also reversely discordant. Three L2 leachates for the Hadean zircon analyzed by Keller et al.
367   (2019) are similarly reversely discordant.
368
369   Reverse discordance in zircon stepwise dissolution experiments is generally attributed to
370   leaching-induced experimental artefacts. Early step-leaching efforts yielded U-Pb isotopic
371   variations that swung wildly between normally and reversely discordant from step-to-step
372   (Todt and Büsch, 1981). Mattinson (1994, 2011) later attributed this effect to the authors'
373   specific dissolution and spiking method which caused U and Pb to fractionate between
374   supernate and U-bearing fluoride precipitates. However, later step-leaching experiments using
375   different experimental procedures also exhibited reverse discordance in early leaching steps
376   (Chen et al., 2001; Mattinson, 2005, 2011). Mattinson (2005, 2011) charged that early leaching
377   steps must reflect a mixture of U and Pb from the dissolved zircon volume plus excess Pb*
378   leached from the intact zircon residue. Mattinson (2005, 2011) further demonstrated that
379   annealing samples at temperatures between 800 - 1100 °C prior to chemical abrasion helped to
380   minimize – but not eliminate – leaching-induced artefacts.
381
382   Reverse discordance is observed naturally in some untreated zircon (Kusiak et al., 2015;
383   Wiemer et al., 2017; Williams et al., 1984). In such cases, reverse discordance is generally
384   attributed to either the internal redistribution of Pb within a crystal or to external factors such
385   as alteration by hydrothermal fluids (Mattinson et al., 1996). Alpha recoil can displace Pb* from
386   the position of its parent radioisotope by ~30 nm (Ewing et al., 2003; Weber, 1990, 1993). In

387 crystals with fine-scale growth zoning, Pb* produced by a U atom within a high-U zone can be
388 implanted into a nearby low-U zone producing a localized occurrence of excess Pb* in the low-
389 U zone (Mattinson et al., 1996). Further, ion imaging and atom probe tomography studies of
390 zircon support the case for nano-to-micro scale Pb redistribution under elevated temperatures
391 and pressures (Kusiak et al., 2015; Peterman et al., 2019, 2021; Reddy et al., 2016). These
392 studies show that unsupported Pb* often forms clusters that are not spatially associated with
393 parent radionuclide growth patterns. However, the exact mechanisms by which Pb* migrates
394 through the zircon structure are poorly understood.
395
396 Notably, our SAM-47 zircon does not exhibit reverse discordance suggesting that only some
397 samples are predisposed to leaching-induced artifacts or leaching-exposed natural U-Pb
398 fractionation. A zircon's U-Pb systematics as revealed by stepwise dissolution must therefore
399 reflect its unique compositional characteristics such as the length-scale and magnitude of
400 radionuclide zonation, the extent of Pb-loss, or the sample's geological history. AS3 is
401 hydrothermally altered, so a component of the reverse discordance observed could potentially
402 reflect the redistribution of Pb isotopes during hydrothermal alteration (Takehara et al., 2018).
403 Why KR18-04 zircon is susceptible to reverse discordance is less clear. Grains appear unaltered
404 and most compositional zones are broad; however, some grains do have thin, high-U zones that
405 could contribute to the internal redistribution of Pb* (McKanna et al., 2023 their Fig. 4 & 15a).
406 Zircon fission track and (U-Th)/He data from Blue Ridge indicate that the region was thermally
407 affected by burial reheating during the late-Paleozoic Alleghenian Orogeny (Naeser et al., 2016;
408 Roden, 1991). Still, there is no evidence that KR18-04 has experienced an extreme high-
409 temperature deformation event. SAM-47 may lack leaching-induced reverse discordance simply
410 because Pb loss in the sample is so pervasive.
411
412 Regardless of the underpinning causes of reverse discordance, this work and that of Mattinson
413 (2005, 2011) demonstrate that increasing the leaching duration and/or temperature helps to
414 eliminate zircon domains affected by open system behavior. These results also highlight that
415 under-leaching samples can produce over-dispersed U-Pb datasets fraught with geologically
416 meaningless analyses. Without the additional context that the 210 °C experiment provides, a
417 researcher could easily interpret the older concordant dates from the 180 °C KR18-04 dataset,
418 for example, as inheritance or prolonged magmatic residence. We stress, however, that our
419 step-wise experiments are under-leached compared to the normal 12 h leaching step used in
420 most labs (see Section 4.3).
421
422 **5.2 The strengths and limitations of geochemical tools for identifying open-system behavior**
423
424 Common Pb and LREEs are incompatible in zircon. Mineral and melt inclusions and
425 hydrothermally altered or metamict zones, however, tend to be enriched in LREEs and common
426 Pb (Bell et al., 2016, 2019). Consequently, geochemical indicators such as a sample's LREE-index
427 (LREE-I = [Dy]/[Nd] + [Dy]/[Sm]) and $Pb*/Pb_c$ (provided demonstrably low laboratory blanks) are
428 useful tools for identifying contamination, hydrothermal alteration, and metamictization.
429 Indeed, our data show that the two variables are generally positively correlated (Fig. 5C, Fig. 6C,
430 and Fig. 7B). Another important geochemical indicator is U concentration – or effective U

concentration (eU = U + 0.235 × Th) – which is a measure of the relative radiation damage in a sample.

These three geochemical indicators are useful tools for evaluating zircon dissolution. In the 180 °C experiments, L1, L2, and some L3 leachates are enriched in LREE, Pb_c, and U relative to zircon residues. Whereas in the 210 °C experiments, L1 and some L2 leachates are enriched in the three variables, however, some L2 and most L3 leachates have compositions similar to residues.

Micro-X-ray computed tomography data presented by McKanna et al. (2023) for AS3 and SAM-47 zircon show that acid readily accesses crystal cores via fractures to dissolve mineral and melt inclusions and strongly metamict zones during L1 at 180 °C and 210 °C. As such, we interpret the LREE, Pb_c, and U enrichment in L1 leachates to reflect the dissolution of inclusions, metamict material, and – in the case of AS3 – hydrothermally altered zones. We attribute LREE, Pb_c, and U enrichments in later leaching steps to the continued dissolution of soluble radiation-damaged or altered domains. KR18-04 zircon grains are more crystalline and typically lack fractures. Consequently, acid only accesses the cores of some grains, and some inclusions armored by highly crystalline material appear to survive twelve hours of chemical abrasion at 180 °C or 210 °C (McKanna et al., 2023). Consequently, LREE and Pb_c enrichment in L2 and L3 leaching steps could reflect later-stage dissolution of inclusions as well as the continued dissolution of radiation-damaged or altered domains.

Comparing leachate and residue chemistry is extremely effective at illuminating the progress of zircon dissolution. However, stepwise chemical abrasion is a time- and labor-intensive process. The overwhelming majority of zircon ID-TIMS U-Pb studies perform single-step chemical abrasion and discard the leachate. Only the residue is characterized. In an ideal scenario, geochemical indicators such as those described here could be used to support the inclusion or exclusion of anomalously young (or old) analyses from geochronological interpretations. Fig. 9 shows ΔAge (Ma) of residues plotted as a function of a grain's LREE-I, $Pb*/Pb_c$, or eU. ΔAge is calculated as the difference between a residue's measured $^{206}Pb/^{238}U$ date and each sample's accepted crystallization age. Negative values for ΔAge reflect Pb loss, while positive values indicate reverse discordance.

Unfortunately, there is no clear correlation between either of the three geochemical indicators and ΔAge in the samples analyzed. Instead, the data suggest that relative enrichments in LREE, Pb_c, and U in residues are not reliable indicators of residual open system behavior. We speculate that the residual zircon affected by open-system behavior is likely volumetrically small compared to the volume of the residual closed-system zircon. Thus, the geochemical signature of the open-system behavior is likely masked by the bulk chemistry of the closed-system residue. Relative enrichments in LREE, Pb_c, and U in residues are likely useful geochemical indicators only if the residual open-system material is proportionally large.

5.3 Leaching temperature and one-step versus stepwise chemical abrasion

474 Stepwise dissolution at 210 °C out-performed stepwise dissolution at 180 °C for all three zircon
475 samples and produced more consistent, concordant datasets. Leaching at 210 °C dissolved
476 zircon material affected by open-system behavior earlier in the leaching process minimizing the
477 frequency and magnitude of normal and reverse discordance compared to the 180 °C
478 experiments (Fig. 1, 2, 3, and 4). The efficacy of the higher leaching temperature is also evident
479 in zircon geochemistry; leaching at 210 °C more efficiently removed zircon material enriched in
480 U, LREE, and Pb_c.
481
482 Notably, U-Pb results for AS3 and KR18-04 residues treated by stepwise dissolution at 180 °C
483 are markedly worse than in previous studies (MacLennan et al., 2020; Schoene et al., 2006).
484 Chemical abrasion of AS3 zircon for 12 to 14 h at 180 °C by Schoene et al. (2006) produced
485 concordant, statistically significant weighted mean U-Pb ages without signs of residual Pb-loss
486 or reverse discordance. Those authors used intensive magnetic separation to target
487 diamagnetic zircon without inclusions, whereas this study included altered grains. While some
488 KR18-04 grains treated at 185 °C for 12 h by (MacLennan et al., 2020) exhibited Pb loss, none of
489 their chemically abraded residues were found to be anomalously old or reversely discordant.
490
491 These apparent discrepancies beg the question: is stepwise dissolution in three 4 h leaching
492 steps equivalent to a single 12 h leaching step? PTFE has a low thermal conductivity making it
493 an effective insulator. To evaluate how temperature in the PTFE-lined Parr pressure dissolution
494 vessel changes with time, a small hole was drilled through the top of an old PTFE liner. The
495 pressure vessel was assembled as normal minus the rupture and corrosion disks. A type-K
496 thermocouple with an insulated wire was threaded through the top of the pressure vessel and
497 into the center of the PTFE liner. The pressure vessel was then placed in a box furnace at 180 °C
498 or 210 °C. Temperature was monitored using a Perfect Prime thermocouple until the
499 temperature in the liner reached equilibrium with the box furnace. The pressure vessel was
500 then removed from the furnace and placed in front of a fan, and temperature was recorded as
501 the pressure vessel cooled to room temperature.
502
503 Results indicate that PTFE is indeed a very effective insulator; the interior of the pressure vessel
504 heats and cools slowly (Fig. 10). It takes 90 to 95 minutes for the interior of the pressure vessel
505 to reach within 20 °C of the target temperature and an additional 30 to 35 minutes to reach
506 within 10 °C of the target temperature. The pressure vessel takes ~90 minutes to cool to room
507 temperature once removed from the oven.
508
509 Given the heating ramp up and cool down times for the PTFE-lined pressure dissolution vessel,
510 samples spend only ~2 h of a 4 h leaching step within 10 °C of the target temperature. As such,
511 a sample leached in three consecutive 4 h steps spends ~6 h within 10 °C of the target
512 temperature. Conversely, a sample leached in a single 12 h step spends ~10 h within 10 °C of
513 the target temperature – ~4 h longer than the step-leached sample. Volume loss estimates for
514 KR18-04 further support this conclusion; volume losses for crystals treated by stepwise
515 chemical abrasion (Fig. 8) are lower than volume losses for crystals chemically abraded for a
516 single 12-h step (McKanna et al., 2023; their Fig. 18).
517

518 We estimate that our dated residues have been leached for a duration equivalent to a single ~8
519 h leaching step on the basis of a 10 °C threshold. Given our U-Pb results, we conclude that
520 zircon chemically abraded at 180 °C for a single 8 h step are "undercooked" and will likely
521 produce data affected by residual Pb-loss and/or leaching-induced artifacts. Unfortunately, we
522 cannot comment on the efficacy of the routinely practiced 12-hour leaching at 180 ˚C used in
523 many labs, except to say it is likely more effective than the results for residues presented here.
524 Zircon samples chemically abraded at 210 °C for a single 8-h leach are likely to produce
525 geologically meaningful results.
526
527 **5.4 The relationships between alpha dose, Pb-loss, and zircon dissolution: Moving toward a**
528 **more predictable model for chemical abrasion**
529
530 Zircon is an outstanding chronometer because radiogenic Pb is immobile in well crystalline
531 zircon (Cherniak et al., 2009; Cherniak and Watson, 2000). Establishing the alpha dose at which
532 radiogenic Pb can mobilize within the zircon structure would help make Pb-loss more
533 predictable. We calculate three different time-integrated alpha doses for each sample using Eq.
534 1 where N_A is Avogadro's number; ^{238}U, ^{235}U, and ^{232}Th are concentrations (ppm) determined
535 for leachates and residues; λ values are the respective decay constants; M values are the
536 respective molar masses (g/mol), and t is the chosen damage accumulation interval (Table 1
537 and Table S3).
538
539 Eq. 1
540
$$\alpha \text{ dose} = \frac{8 \cdot N_A \cdot {}^{238}U}{M_{238} \cdot 10^6} \cdot (e^{\lambda_{238} t} - 1) + \frac{7 \cdot N_A \cdot {}^{235}U}{M_{235} \cdot 10^6} \cdot (e^{\lambda_{235} t} - 1) + \frac{6 \cdot N_A \cdot {}^{232}Th}{M_{232} \cdot 10^6} \cdot (e^{\lambda_{232} t} - 1)$$

541
542 "Total" alpha dose assumes a damage accumulation interval equivalent to a sample's
543 crystallization age. This calculation ignores the possibility of radiation damage annealing.
544 "Present day" alpha dose estimates attempt to take geological annealing into account.
545 Radiation damage anneals at temperatures above ~200 to 300°C on geological timescales
546 (Bernet, 2009; Yamada et al., 2007). The closure temperature for the (U-Th)/He system in
547 crystalline zircon is ~180 °C (Guenthner et al., 2013; Reiners et al., 2004). As such, we use
548 published zircon (U-Th)/He dates or thermal histories derived from zircon (U-Th)/He datasets
549 for the Minnesota River Valley (Guenthner et al., 2013; McDannell et al., 2022), the Eastern
550 Pilbara craton (Magee et al., 2017), and the Virginia Blue Ridge (Basler et al., 2021) to estimate
551 minimum damage accumulation intervals for samples' "present day" alpha doses. Since zircon
552 (U-Th)/He dates for the Eastern Pilbara craton broadly overlap the lower-intercept U-Pb
553 concordia age for SAM-47, we take the lower-intercept age as the damage accumulation
554 interval. Chosen intervals for "present day" alpha doses for AS3, SAM-47, and KR18-04 are 750
555 Ma, 751 Ma, and 298 Ma, respectively.
556
557 "Present day" alpha dose estimates can also be established independently using Raman
558 spectroscopy, since key bands in the zircon Raman spectrum broaden predictably with
559 increasing alpha dose (Nasdala et al., 2001; Palenik et al., 2003). "Present day" alpha doses for
560 AS3 and SAM-47 closely match Raman-based alpha doses (α_r) determined by McKanna et al.

561 (2023) for zircon from the same sample aliquots (Table 1). "Present day" alpha doses for KR18-
562 04 have a similar lower bound but a higher upper bound compared to Raman estimates
563 (McKanna et al., 2023). Most likely, Raman measurements failed to capture volumetrically
564 small, higher-U domains such as the thin concentric dissolution features evident in secondary
565 electron images of KR18-04 residues (McKanna et al., 2023, their Fig. 15a-I reproduced here in
566 Fig. 13b).

568 The final calculation estimates alpha dose at the time of Pb-loss. Because AS3 and KR18-04
569 exhibit zero-age Pb-loss, "present day" and "Pb-loss" alpha doses estimates are equivalent. The
570 Pb-loss discord for SAM-47, however, suggests that Pb-loss occurred in the distant geological
571 past at or before 751 ± 140 Ma (Fig. 3C). Therefore, the maximum "Pb-loss" damage
572 accumulation interval is the difference between the sample's upper and lower intercept ages
573 which equates to ~2571 Ma.

575 Fig. 11 shows the distribution of "Pb-loss" alpha dose estimates for all leachates affected by Pb-
576 loss. Despite vastly different geological settings and ranges in radiation damage densities,
577 leachates affected by Pb-loss exhibit similar alpha dose distributions. The majority have alpha
578 doses that are $\geq 6 \times 10^{17}$ α/g. We therefore establish this alpha dose as our best estimate for
579 the threshold above which Pb can mobilize within the zircon structure. The mechanism that
580 mobilizes Pb – diffusion, leaching, or recrystallization – is not clear, however, fluids likely play
581 an important role. As such, while zircon with alpha doses above 6×10^{17} α/g may be *susceptible*
582 to Pb loss, not all damaged grains will be affected by open system behavior. Notably, the 6 ×
583 10^{17} α/g threshold is somewhat lower than the alpha dose – 1×10^{18} α/g – at which zircon
584 material properties such as density begin to change (Ewing et al., 2003; Nasdala et al., 2004).
585 However, the 6×10^{17} α/g threshold is similar to some estimates for the alpha dose at which
586 helium diffusion begins to increase causing the closure temperature for He in zircon to decrease
587 (Anderson et al., 2017, 2020).

588 For the best geochronological outcomes, chemical abrasion should target zircon material
589 susceptible to Pb-loss, i.e., material with alpha doses above 6×10^{17} α/g . Fig. 12 shows
590 "present day" alpha dose estimates for all leachates and residues from the 180 °C and 210 °C
591 experiments. The apparent differences in alpha dose between the two leaching temperatures
592 reflects the fraction of material dissolved in each step. At 180 °C, smaller volumes of high-U
593 zones dissolve, whereas at 210 °C larger volumes of material including both high-U and
594 medium-U zones dissolve causing average alpha doses to be lower in the 210 °C dataset.

595 In the 180 °C experiments, the median alpha dose decreases with increasing leaching duration
596 consistent with the expected effects of radiation damage on zircon solubility (Fig. 12). A
597 majority of residues from the 180 °C experiments have alpha doses > 6×10^{17} α/g suggesting
598 that residues may be affected by residual open system behavior in agreement with our U-Pb
599 isotopic results. Evidently, dissolving zircon with lower alpha doses requires longer leaching
600 durations at 180 °C than achieved in this study, which was equivalent to a single 8-hour leach
601 step. In contrast, the median alpha dose for residues as well as L2 and L3 leachates from the

602 210 °C experiments have alpha doses below the established threshold. Zircon material with
603 alpha doses ≥ 6 × 10^{17} α/g is thus readily dissolved at short leaching durations at 210 °C.

604 Framing Pb loss and zircon solubility in terms of alpha dose allows a user to better predict how
605 chemical abrasion might affect a specific zircon dataset. Chemical abrasion is a time-consuming
606 method that is applied to the majority of ID-TIMS U-Pb datasets, but it may be unnecessary for
607 low-alpha dose, inclusion-free zircon. Further, by estimating a sample's "present day" alpha
608 dose distribution, a user can better anticipate how a sample will dissolve (McKanna et al.,
609 2023). For example, if a sample has accumulated a lot of radiation damage like SAM-47,
610 leaching longer than a single 8-h step at 210 °C will likely leave little to no residue for isotopic
611 analysis. Whereas, if a sample has a lower average alpha dose like KR18-04, a longer 210 °C
612 leach is likely safe and potentially more effective.

614 Determining alpha dose prior to dissolution, however, remains an outstanding challenge.
615 Raman spectroscopy is one method that can be used to estimate alpha dose (Nasdala et al.,
616 2001; Palenik et al., 2003). Alpha dose can also be estimated from laser ablation ICPMS U-Pb
617 data, since laser ablation U-Pb analysis is often used for pre-screening grains for ID-TIMS U-Pb
618 dating. Unfortunately, both methods are time- and resource-intensive. Fig. 13 plots alpha dose
619 as a function of time for different U concentrations. As described above, different time intervals
620 can be selected for damage accumulation depending on the calculation's goal. This figure is a
621 simple visual representation that can help a researcher determine whether or not a sample is
622 likely to be susceptible to Pb loss given a range of possible U concentrations and a rough
623 estimate for the sample's damage accumulation interval.

625 As highlighted in Fig. 13b, perhaps the most persistent challenge when it comes to tailoring
626 chemical abrasion for a specific zircon dataset are crystal-specific factors such as the spatial
627 distribution and magnitude of intracrystalline variations in radiation damage, inclusions, and
628 fractures which strongly affect how a zircon dissolves as discussed in our companion paper
629 (McKanna et al., 2023). While micro-X-ray computed tomography can visualize inclusions and
630 fractures in zircon in three-dimensions (3D) (McKanna et al., 2023), at present, no method
631 exists for quantifying radiation damage zonation in 3D. Radionuclide zoning explains the
632 inconsistent dissolution behavior evidenced in Fig. 8. For example, the percent zircon dissolved
633 in each leaching step decreases from L1 to L3 for AS3 zircon, remains constant or decreases for
634 SAM-47 zircon, and remains constant or increases for KR18-04 zircon. This inconsistent
635 behavior occurs because the percent zircon dissolved is not only a function of alpha dose, but
636 also 1) the volumetric proportion of zircon with a given alpha dose, and 2) which portions of a
637 crystal are in contact with HF at any given time during the leaching process. Building a
638 comprehensive model for chemical abrasion will ultimately require both geochemical and
639 textural inputs.

641 **6. Conclusions**

643 Single-crystal stepwise dissolution experiments performed at 180 °C and 210°C provide new
644 insights into the geochronological and geochemical effects of chemical abrasion on zircon

645 datasets. Because of the insulating properties of the PTFE-lined pressure dissolution vessel,
646 stepwise dissolution in three 4-h leaching steps is not equivalent to a 12-h single-step chemical
647 abrasion, the method most commonly used by the zircon ID-TIMS U-Pb community. We
648 estimate that our stepwise dissolution approach is roughly equivalent to 8-h single-step
649 chemical abrasion. Stepwise dissolution at 180 °C produced over-dispersed U-Pb datasets
650 affected by both residual Pb-loss and leaching-induced or leaching-exposed artefacts which
651 present as reverse discordance. Without the context of the 210 °C results, reverse discordance
652 in the 180 °C datasets could easily be mistaken for prolonged crystallization or inheritance and
653 lead to spurious geological interpretations. Longer leaching durations are likely needed to
654 produce robust geochronological datasets at 180 °C.
655
656 Stepwise dissolution at 210 °C outperformed the 180 °C experiments by all measures for the
657 three zircon samples analyzed producing more reproducible, concordant results. Ultimately,
658 how a zircon sample responds to any chemical abrasion protocol will be sample-dependent.
659 However, our results suggest that 8-h single-step chemical abrasion at 210 °C may be effective
660 at mitigating Pb-loss and reverse discordance for a wide range of zircon samples. Further study
661 of different zircon samples is needed. Our results, however, clearly demonstrate that leaching
662 durations longer than an 8-h single step are required for chemical abrasion at 180 °C to be
663 effective.
664
665 U concentration, Pb*/Pb$_c$, and LREE enrichment are useful tools for tracking the dissolution of
666 inclusions and radiation-damaged or altered material during stepwise dissolution. These
667 geochemical indicators, however, are not effective at identifying residual Pb-loss in the zircon
668 residues analyzed.
669
670 We attempted to constrain the relationship between Pb-loss and radiation damage by
671 calculating an alpha dose for each leachate based on its measured radionuclide concentration
672 and an estimated damage accumulation interval informed by the sample's geologic history.
673 "Pb-loss" alpha dose estimates suggest that Pb may mobilize within the zircon structure at
674 alpha doses as low as 6×10^{17} α/g. "Present day" alpha dose estimates indicate that many
675 residues treated by stepwise dissolution at 180 °C have alpha doses above the 6×10^{17} α/g
676 threshold, and consequently, many 180 °C residues are affected by residual Pb-loss. The
677 majority of residues treated at 210 °C – and many L2 and L3 leachates – have "present day"
678 alpha doses below this threshold. Grains expected to have accumulated alpha doses $< 6 \times 10^{17}$
679 α/g based on expected radionuclide concentrations and damage accumulation intervals are
680 unlikely to be affected by Pb-loss and may not require chemical abrasion. However, chemical
681 abrasion may help improve the precision of U-Pb analyses even in low-damage grains by
682 dissolving Pb$_c$-bearing inclusions. The effectiveness of any chemical abrasion protocol will
683 ultimately be sample-dependent, since zircon dissolution depends not only on a grain's bulk
684 chemistry, but also the spatial distribution and magnitude of intracrystalline variations in
685 radiation damage.

686 **Data availability.** All data presented are included in this paper or the Supplement.

687 **Supplement.** The supplement related to this article is available online at:

688 **Author contributions.** AJM carried out the experiments and wrote the manuscript. All authors –
689 AJM, DS, and BS – contributed to the experiment design and data reduction, interpretation, and
690 presentation.

691 **Competing interests.** The contact author has declared that none of the authors has any
692 competing interests.

693 **Disclaimer.** Publisher's note: Copernicus Publications remains neutral with regard to
694 jurisdictional claims in published maps and institutional affiliations.

695 **Acknowledgements.** Thank you to Mami Takehara of the National Institute of Polar Research in
696 Tokyo, Japan, for providing the hydrothermally altered AS3 zircon crystals used in this study.
697 We would like to thank Fernando Corfu and an anonymous reviewer for their thoughtful
698 feedback that helped to improve this manuscript.

699 **Financial support.** This work was supported by research funds provided by the Department of
700 Geosciences at Princeton University granted to Alyssa J. McKanna as part of her Harry Hess
701 Postdoctoral Fellowship.

702 **Review statement.**

703 **References**
704
705 Anderson, A. J., Hodges, K. V., & van Soest, M. C. (2017). Empirical constraints on the effects of
706   radiation damage on helium diffusion in zircon. *Geochimica et Cosmochimica Acta*, *218*,
707   308–322. https://doi.org/10.1016/j.gca.2017.09.006
708 Anderson, A. J., van Soest, M. C., Hodges, K. V., & Hanchar, J. M. (2020). Helium diffusion in
709   zircon: Effects of anisotropy and radiation damage revealed by laser depth profiling.
710   *Geochimica et Cosmochimica Acta*, *274*, 45–62. https://doi.org/10.1016/j.gca.2020.01.049
711 Barley, M. E., & Pickard, A. L. (1999). 41-62 An extensive, crustally-derived. In *Precambrian*
712   *Research* (Vol. 96).
713 Basler, L. C., Baughman, J. S., Fame, M. L., & Haproff, P. J. (2021). Spatially variable syn- and
714   post-Alleghanian exhumation of the central Appalachian Mountains from zircon (U-Th)/He
715   thermochronology. *Geosphere*, *17*(4), 1151–1169. https://doi.org/10.1130/GES02368.1
716 Bell, E. A., Boehnke, P., Barboni, M., & Harrison, T. M. (2019). Tracking chemical alteration in
717   magmatic zircon using rare earth element abundances. *Chemical Geology*, *510*, 56–71.
718   https://doi.org/10.1016/j.chemgeo.2019.02.027
719 Bell, E. A., Boehnke, P., & Harrison, T. M. (2016). Recovering the primary geochemistry of Jack
720   Hills zircons through quantitative estimates of chemical alteration. *Geochimica et*
721   *Cosmochimica Acta*, *191*, 187–202. https://doi.org/10.1016/j.gca.2016.07.016
722 Bernet, M. (2009). A field-based estimate of the zircon fission-track closure temperature.
723   *Chemical Geology*, *259*(3–4), 181–189. https://doi.org/10.1016/j.chemgeo.2008.10.043

724 Bowring, J. F., McLean, N. M., & Bowring, S. A. (2011). Engineering cyber infrastructure for U-Pb
725   geochronology: Tripoli and U-Pb-Redux. *Geochemistry, Geophysics, Geosystems*, *12*(6).
726   https://doi.org/10.1029/2010GC003479
727 Chen, F., Siebel, W., & Satir, M. (2001). Zircon U-Pb and Pb-isotope fractionation during
728   stepwise HF acid leaching and geochronological implications. In *Chem. Geol* (Vol. 172).
729   www.elsevier.com/locate/chemgeo
730 Cherniak, D. J., & Watson, E. B. (2000). Pb diffusion in zircon. *Chemical Geology*, *172*, 5–24.
731   www.elsevier.comrlocaterchemgeo
732 Cherniak, D. J., Watson, E. B., & Thomas, J. B. (2009). Diffusion of helium in zircon and apatite.
733   *Chemical Geology*, *268*(1–2), 155–166. https://doi.org/10.1016/j.chemgeo.2009.08.011
734 Condon, D. J., Schoene, B., McLean, N. M., Bowring, S. A., & Parrish, R. R. (2015). Metrology and
735   traceability of U-Pb isotope dilution geochronology (EARTHTIME Tracer Calibration Part I).
736   *Geochimica et Cosmochimica Acta*, *164*, 464–480.
737   https://doi.org/10.1016/j.gca.2015.05.026
738 Corfu, F. (2013). A century of U-pb geochronology: The long quest towards concordance. In
739   *Bulletin of the Geological Society of America* (Vol. 125, Issues 1–2, pp. 33–47).
740   https://doi.org/10.1130/B30698.1
741 Davis, D. W., & Krogh, T. E. (2000). Preferential dissolution of 234 U and radiogenic Pb from a-
742   recoil-damaged lattice sites in zircon: implications for thermal histories and Pb isotopic
743   fractionation in the near surface environment. In *Chemical Geology* (Vol. 172).
744   www.elsevier.comrlocaterchemgeo
745 Ewing, R. C., Meldrum, A., Wang, L., Weber, W. J., & Corrales, L. R. (2003). Radiation Effects in
746   Zircon. *Reviews in Mineralogy and Geochemistry*, *53*(1), 387–425.
747   https://doi.org/10.2113/0530387
748 Geisler, T., Pidgeon, R. T., van Bronswijk, W., & Kurtz, R. (2002). Transport of uranium, thorium,
749   and lead in metamict zircon under low-temperature hydrothermal conditions. *Chemical*
750   *Geology*, *191*, 141–154. www.elsevier.com/locate/chemgeo
751 Gerstenberger, H., & Haase, G. (1997). A highly effective emitter substance for mass
752   spectrometric Pb isotope ratio determinations. In *Chemical Geology* (Vol. 136).
753 Guenthner, W. R., Reiners, P. W., Ketcham, R. A., Nasdala, L., & Giester, G. (2013). Helium
754   diffusion in natural zircon: radiation damage, anisotropy, and the interpretation of zircon
755   (U-TH)/He thermochronology. *American Journal of Science*, *313*(3), 145–198.
756   https://doi.org/10.2475/03.2013.01
757 Heiss, J., Condon, D. J., McLean, N., & Noble, S. R. (2012). 238U/235U Systematics in Terrestrial
758   Uranium-Bearing Minerals. *Science*, *335*(6076), 1610–1613.
759 Huyskens, M. H., Zink, S., & Amelin, Y. (2016). Evaluation of temperature-time conditions for
760   the chemical abrasion treatment of single zircons for U-Pb geochronology. *Chemical*
761   *Geology*, *438*, 25–35. https://doi.org/10.1016/j.chemgeo.2016.05.013
762 Jaffey, A. H., Flynn, K. F., Glendenin, L. E., Bentley, W. C., & Essling, A. M. (1971). Precision
763   Measurement of Half-Lives and Specific Activities of 235U and 238U. *Physical Review C*,
764   *4*(5), 1889–1906. https://doi.org/10.1103/PhysRevC.4.1889
765 Keller, B. (2023). Technical Note: Pb-loss-aware Eruption/Deposition Age Estimation. *GChron*,
766   *Preprint*. https://doi.org/10.5194/gchron-2023-9

767   Keller, B. C., Boehnke, P., Schoene, B., & Harrison, T. M. (2019). Stepwise chemical abrasion-
768   isotope dilution-thermal ionization mass spectrometry with trace element analysis of
769   microfractured Hadean zircon. *Geochronology*, *1*(1), 85–97.
770   https://doi.org/10.5194/gchron-1-85-2019
771   Kloppenburg, A. (2003). *Structural evolution of the Marble Bar Domain, Pilbara granite-*
772   *greenstone terrain, Australia : the role of Archaean mid-crustal detachments = Structurele*
773   *evolutie van het Marble Bar Domein, Pilbara graniet-groensteen terrein, Australie : de rol*
774   *van Archaeische decollements in de middenkorst* [PhD Dissertation]. Utrecht University.
775   Kloppenburg, A., White, S. H., & Zegers, T. E. (2001). Structural evolution of the Warrawoona
776   Greenstone Belt and adjoining granitoid complexes, Pilbara Craton, Australia: implications
777   for Archaean tectonic processes. In *Precambrian Research* (Vol. 112).
778   www.elsevier.com/locate/precamres
779   Krogh, T. E. (1973). A low-contamination method for hydrothermal decomposition of zircon and
780   extraction of U and Pb for isotopic age determinations. *Geochimica et Cosmochimica Acta*,
781   *37*, 485–494.
782   Krogh, T. E. (1981). Improved accuracy of U-Pb zircon ages by the creation of more concordant
783   systems using an air abrasion technique. *Geochimica et Cosmochimico Acta*, *46*, 637–649.
784   Kusiak, M. A., Dunkley, D. J., Wirth, R., Whitehouse, M. J., Wilde, S. A., & Marquardt, K. (2015).
785   Metallic lead nanospheres discovered in ancient zircons. *Proceedings of the National*
786   *Academy of Sciences of the United States of America*, *112*(16), 4958–4963.
787   https://doi.org/10.1073/pnas.1415264112
788   MacLennan, S. A. (2019). *Temporal constraints on Archean crustal geodynamics and*
789   *Neoproterozoic glaciation* [PhD Dissertation]. Princeton University.
790   MacLennan, S. A., Eddy, M. P., Merschat, A. J., Mehra, A. K., Crockford, P. W., Maloof, A. C.,
791   Southworth, C. S., & Schoene, B. (2020). Geologic evidence for an icehouse Earth before
792   the Sturtian global glaciation. *Science Advances*, *6*(24).
793   https://doi.org/10.1126/sciadv.aay6647
794   Magee, C. W., Danišík, M., & Mernagh, T. (2017). Extreme isotopologue disequilibrium in
795   molecular SIMS species during SHRIMP geochronology. *Geoscientific Instrumentation,*
796   *Methods and Data Systems*, *6*(2), 523–536. https://doi.org/10.5194/gi-6-523-2017
797   Mattinson, J. M. (1994). Mineralogy and Petrology A study of complex discordance in zircons
798   using step-wise dissolution techniques. *Contributions to Mineralogy and Petrology*, *116*,
799   117–129.
800   Mattinson, J. M. (2005). Zircon U-Pb chemical abrasion ("CA-TIMS") method: Combined
801   annealing and multi-step partial dissolution analysis for improved precision and accuracy
802   of zircon ages. *Chemical Geology*, *220*(1–2), 47–66.
803   https://doi.org/10.1016/j.chemgeo.2005.03.011
804   Mattinson, J. M. (2011). Extending the Krogh legacy: development of the CA–TIMS method for
805   zircon U–Pb geochronologyThis article is one of a series of papers published in this Special
806   Issue on the theme of *Geochronology* in honour of Tom Krogh. *Canadian Journal of Earth*
807   *Sciences*, *48*(2), 95–105. https://doi.org/10.1139/E10-023
808   Mattinson, J. M., Graubard, C. M., Parkinson, D. L., & McClelland, W. C. (1996). U-Pb Reverse
809   Discordance in Zircons: The Role of Fine-Scale Oscillatory Zoning and Sub-Micron Transport

810   of Pb. In A. Basu & S. Hart (Eds.), *Earth Processes: Reading the Isotopic Code* (pp. 355–370).
811   AGU. https://doi.org/10.1029/GM095p0355

812 McDannell, K. T., Keller, C. B., Guenthner, W. R., Zeitler, P. K., & Shuster, D. L. (2022).
813   Thermochronologic constraints on the origin of the Great Unconformity. *Proceedings of*
814   *the National Academy of Sciences*, *119*(5). https://doi.org/10.1073/pnas.2118682119

815 McKanna, A. J., Koran, I., Schoene, B., & Ketcham, R. A. (2023). Chemical abrasion: the
816   mechanics of zircon dissolution. *Geochronology*, *5*(1), 127–151.
817   https://doi.org/10.5194/gchron-5-127-2023

818 McLean, N. M., Bowring, J. F., & Bowring, S. A. (2011). An algorithm for U-Pb isotope dilution
819   data reduction and uncertainty propagation. *Geochemistry, Geophysics, Geosystems*,
820   *12*(6). https://doi.org/10.1029/2010GC003478

821 McLean, N. M., Condon, D. J., Schoene, B., & Bowring, S. A. (2015). Evaluating uncertainties in
822   the calibration of isotopic reference materials and multi-element isotopic tracers
823   (EARTHTIME Tracer Calibration Part II). *Geochimica et Cosmochimica Acta*, *164*, 481–501.
824   https://doi.org/10.1016/j.gca.2015.02.040

825 Meldrum, A., Boatner, L. A., Weber, W. J., & Ewing, R. C. (1998). Radiation damage in zircon and
826   monazite. *Geochimica et Cosmochimica Acta*, *62*(14), 2509–2520.

827 Merschat, A. J., Southworth, S., McClellan, E., Tollo, R. P., Rankin, D. W., Hooper, S., & Bauer, S.
828   (2014). Key structural and stratigraphic relationships from the northeast end of the
829   Mountain City window and the Mount Rogers area, Virginia–North Carolina–Tennessee. In
830   *Elevating Geoscience in the Southeastern United States: New Ideas about Old Terranes—*
831   *Field Guides for the GSA Southeastern Section Meeting, Blacksburg, Virginia, 2014* (pp. 63–
832   101). Geological Society of America. https://doi.org/10.1130/2014.0035(03)

833 Mezger, K., & Krogstad, E. J. (1997). Interpretation of discordant U-Pb zircon ages: An
834   evaluation. *Journal of Metamorphic Geology*, *15*(1), 127–140.
835   https://doi.org/10.1111/j.1525-1314.1997.00008.x

836 Miller, J. S., Matzel, J. E. P., Miller, C. F., Burgess, S. D., & Miller, R. B. (2007). Zircon growth and
837   recycling during the assembly of large, composite arc plutons. *Journal of Volcanology and*
838   *Geothermal Research*, *167*(1–4), 282–299.
839   https://doi.org/10.1016/j.jvolgeores.2007.04.019

840 Moore, W. B., & Webb, A. A. G. (2013). Heat-pipe Earth. *Nature*, *501*(7468), 501–505.
841   https://doi.org/10.1038/nature12473

842 Morón, S., Kohn, B. P., Beucher, R., Mackintosh, V., Cawood, P. A., Moresi, L., & Gallagher, S. J.
843   (2020). Denuding a Craton: Thermochronology Record of Phanerozoic Unroofing From the
844   Pilbara Craton, Australia. *Tectonics*, *39*(9). https://doi.org/10.1029/2019TC005988

845 Mundil, R., Ludwig, K. R., Metcalfe, I., & Renne, P. R. (2004). Age and Timing of the Permian
846   Mass Extinctions: U/Pb Dating of Closed-System Zircons. *Science*, *305*, 1760–1762.
847   www.sciencemag.org

848 Naeser, C. W., Naeser, N. D., Newell, W. L., Southworth, S., Edwards, L. E., & Weems, R. E.
849   (2016). Erosional and depositional history of the Atlantic passive margin as recorded in
850   detrital zircon fission-track ages and lithic detritus in Atlantic Coastal plain sediments.
851   *American Journal of Science*, *316*(2), 110–168. https://doi.org/10.2475/02.2016.02

852 Nasdala, L., Reiners, P. W., Garver, J. I., Kennedy, A. K., Stern, R. A., Balan, E., & Wirth, R. (2004).
853   Incomplete retention of radiation damage in zircon from Sri Lanka. *American Mineralogist*,
854   *89*, 219–231.
855 Nasdala, L., Wenzel, M., Vavra, G., Irmer, G., Wenzel, T., & Kober, B. (2001). Metamictisation of
856   natural zircon: Accumulaton versus thermal annealing of radioactivity-induced damage.
857   *Contributions to Mineralogy and Petrology*, *141*(2), 125–144.
858   https://doi.org/10.1007/s004100000235
859 O'Connor, L., Szymanowski, D., Eddy, M. P., Samperton, K. M., & Schoene, B. (2022). A red bole
860   zircon record of cryptic silicic volcanism in the Deccan Traps, India. *Geology*, *50*(4), 460–
861   464. https://doi.org/10.1130/G49613.1
862 Paces, J. B., & Miller, J. D. (1993). Precise U-Pb ages of Duluth Complex and related mafic
863   intrusions, northeastern Minnesota: geochronological insights to physical, petrogenetic,
864   paleomagnetic, and tectonomagmatic processes associated with the 1.1 Ga Midcontinent
865   Rift system. *Journal of Geophysical Research*, *98*(B8). https://doi.org/10.1029/93jb01159
866 Palenik, C. S., Nasdala, L., & Ewing, R. C. (2003). Radiation damage in zircon. *American
867   Mineralogist*, *88*, 770–781.
868 Peterman, E. M., Reddy, S. M., Saxey, D. W., Fougerouse, D., Snoeyenbos, D. R., & Rickard, W.
869   D. A. (2019). Nanoscale processes of trace element mobility in metamorphosed zircon.
870   *Contributions to Mineralogy and Petrology*, *174*(11). https://doi.org/10.1007/s00410-019-
871   1631-1
872 Peterman, E. M., Reddy, S. M., Saxey, D. W., Fougerouse, D., Zakaria Quadir, M., & Jercinovic,
873   M. J. (2021). Trace-element segregation to dislocation loops in experimentally heated
874   zircon. *American Mineralogist*, *106*(12), 1971–1979. https://doi.org/10.2138/am-2021-
875   7654
876 Reddy, S. M., van Riessen, A., Saxey, D. W., Johnson, T. E., Rickard, W. D. A., Fougerouse, D.,
877   Fischer, S., Prosa, T. J., Rice, K. P., Reinhard, D. A., Chen, Y., & Olson, D. (2016).
878   Mechanisms of deformation-induced trace element migration in zircon resolved by atom
879   probe and correlative microscopy. *Geochimica et Cosmochimica Acta*, *195*, 158–170.
880   https://doi.org/10.1016/j.gca.2016.09.019
881 Reiners, P. W., Spell, T. L., Nicolescu, S., & Zanetti, K. A. (2004). Zircon (U-Th)/He
882   thermochronometry: He diffusion and comparisons with 40Ar/39Ar dating. *Geochimica et
883   Cosmochimica Acta*, *68*(8), 1857–1887. https://doi.org/10.1016/j.gca.2003.10.021
884 Roden, M. K. (1991). Apatite Fission-Track Thermochronology of the Southern Appalachian
885   Basin: Maryland, West Virginia, and Virginia. *The Journal of Geology*, *99*(1), 41–53.
886   https://doi.org/10.1086/629472
887 Schmitz, M. D., Bowring, S. A., & Ireland, T. R. (2003). *Evaluation of Duluth Complex anorthositic
888   series (AS3) zircon as a U-Pb geochronological standard: New high-precision isotope
889   dilution thermal ionization mass spectrometry results*. https://doi.org/10.1016/S0016-
890   7037(00)00200-X
891 Schoene, B. (2014). U–Th–Pb Geochronology. In *Treatise on Geochemistry* (pp. 341–378).
892   Elsevier. https://doi.org/10.1016/B978-0-08-095975-7.00310-7
893 Schoene, B., Crowley, J. L., Condon, D. J., Schmitz, M. D., & Bowring, S. A. (2006). Reassessing
894   the uranium decay constants for geochronology using ID-TIMS U-Pb data. *Geochimica et
895   Cosmochimica Acta*, *70*(2), 426–445. https://doi.org/10.1016/j.gca.2005.09.007

Schoene, B., Latkoczy, C., Schaltegger, U., & Günther, D. (2010). A new method integrating high-precision U-Pb geochronology with zircon trace element analysis (U-Pb TIMS-TEA). *Geochimica et Cosmochimica Acta*, *74*(24), 7144–7159. https://doi.org/10.1016/j.gca.2010.09.016

Smithies, R. H., Champion, D. C., & Cassidy, K. F. (2003). Formation of Earth's early Archaean continental crust. *Precambrian Research*, *127*(1–3), 89–101. https://doi.org/10.1016/S0301-9268(03)00182-7

Swanson-Hysell, N. L., Hoaglund, S. A., Crowley, J. L., Schmitz, M. D., Zhang, Y., & Miller, J. D. (2020). Rapid emplacement of massive Duluth Complex intrusions within the North American Midcontinent Rift. *Geology*, *49*(2), 185–189. https://doi.org/10.1130/G47873.1

Swanson-Hysell, N. L., Ramezani, J., Fairchild, L. M., & Rose, I. R. (2019). Failed rifting and fast drifting: Midcontinent Rift development, Laurentia's rapid motion and the driver of Grenvillian orogenesis. *Bulletin of the Geological Society of America*, *131*(5–6), 913–940. https://doi.org/10.1130/B31944.1

Szymanowski, D., & Schoene, B. (2020). U–Pb ID-TIMS geochronology using ATONA amplifiers. *Journal of Analytical Atomic Spectrometry*, *35*(6), 1207–1216. https://doi.org/10.1039/D0JA00135J

Takehara, M., Horie, K., Hokada, T., & Kiyokawa, S. (2018). New insight into disturbance of U-Pb and trace-element systems in hydrothermally altered zircon via SHRIMP analyses of zircon from the Duluth Gabbro. *Chemical Geology*, *484*, 168–178. https://doi.org/10.1016/j.chemgeo.2018.01.028

Todt, W. A., & Büsch, W. (1981). U-Pb investigations on zircons from pre-Variscan gneisses-I. A study from the Schwarzwald, West Germany. *Geochimica et Cosmochimica Acta*, *45*, 1789–1801.

Van Kranendonk, M. J., Hugh Smithies, R., Hickman, A. H., & Champion, D. C. (2007). Review: Secular tectonic evolution of Archean continental crust: interplay between horizontal and vertical processes in the formation of the Pilbara Craton, Australia. In *Terra Nova* (Vol. 19, Issue 1, pp. 1–38). https://doi.org/10.1111/j.1365-3121.2006.00723.x

Weber, W. J. (1990). Radiation-induced defects and amorphization in zircon. *J. Mater. Res.*, *5*(11), 2687–2697. http://journals.cambridge.org

Weber, W. J. (1993). Alpha-Decay-Induced Amorphization in Complex Silicate Structures. *Journal of the American Ceramic Society*, *76*(7), 1729–1738. https://doi.org/10.1111/j.1151-2916.1993.tb06641.x

Widmann, P., Davies, J. H. F. L., & Schaltegger, U. (2019). Calibrating chemical abrasion: Its effects on zircon crystal structure, chemical composition and U–Pb age. *Chemical Geology*, *511*, 1–10. https://doi.org/10.1016/j.chemgeo.2019.02.026

Wiemer, D., Allen, C. M., Murphy, D. T., & Kinaev, I. (2017). Effects of thermal annealing and chemical abrasion on ca. 3.5 Ga metamict zircon and evidence for natural reverse discordance: Insights for U[sbnd]Pb LA-ICP-MS dating. *Chemical Geology*, *466*, 285–302. https://doi.org/10.1016/j.chemgeo.2017.06.019

Williams, I. S., Compston, W., Black, L. P., Ireland, T. R., & Foster, J. J. (1984). Contributions to Mineralogy and Petrology Unsupported radiogenic Pb in zircon: a cause of anomalously high Pb-Pb, U-Pb and Th-Pb ages. In *Contrib Mineral Petrol* (Vol. 88).

939   Yamada, R., Murakami, M., & Tagami, T. (2007). Statistical modelling of annealing kinetics
940   of fission tracks in zircon; Reassessment of laboratory experiments. *Chemical*
941   *Geology*, *236*(1–2), 75–91. https://doi.org/10.1016/j.chemgeo.2006.09.002

942
943
944
945
946
947
948
949
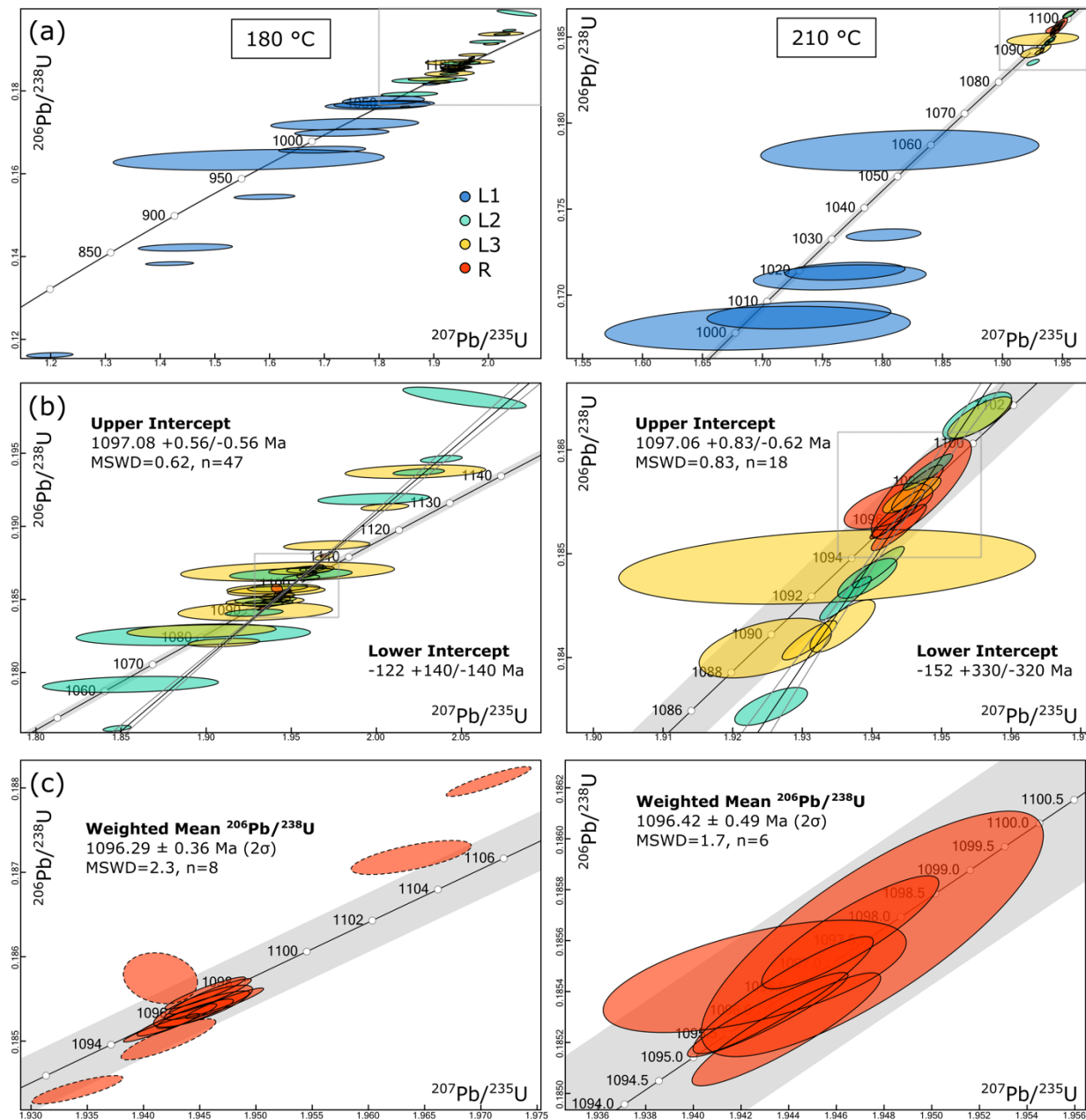
Figure 1. U-Pb concordia diagrams for the 180 °C (left) and 210 °C (right) AS3 experiments. **(a)** All data are depicted except for L1 leachates with Pb*/Pb$_c$ values < 1. **(b)** Close up of L2, L3, and R data. **(c)** Close up of zircon residue data. Ellipses with dashed borders were excluded from the weighted-mean ^{206}Pb/^{238}U age for the 180 °C experiment. All ellipses reflect 2σ analytical uncertainties.

950
951
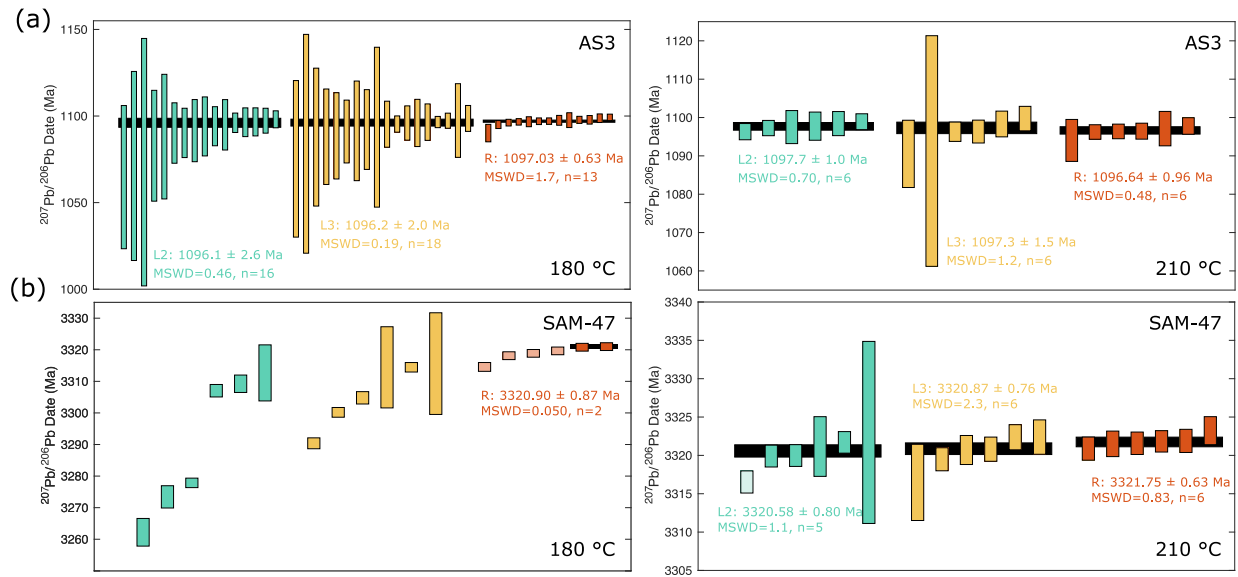
Figure 2. Ranked order ^{207}Pb/^{206}Pb dates for the **(a)** AS3 and **(b)** SAM-47 experiments. Black bars represent weighted means. Bar heights and quoted uncertainties reflect propagated 2σ analytical uncertainties.

952
953
954
955
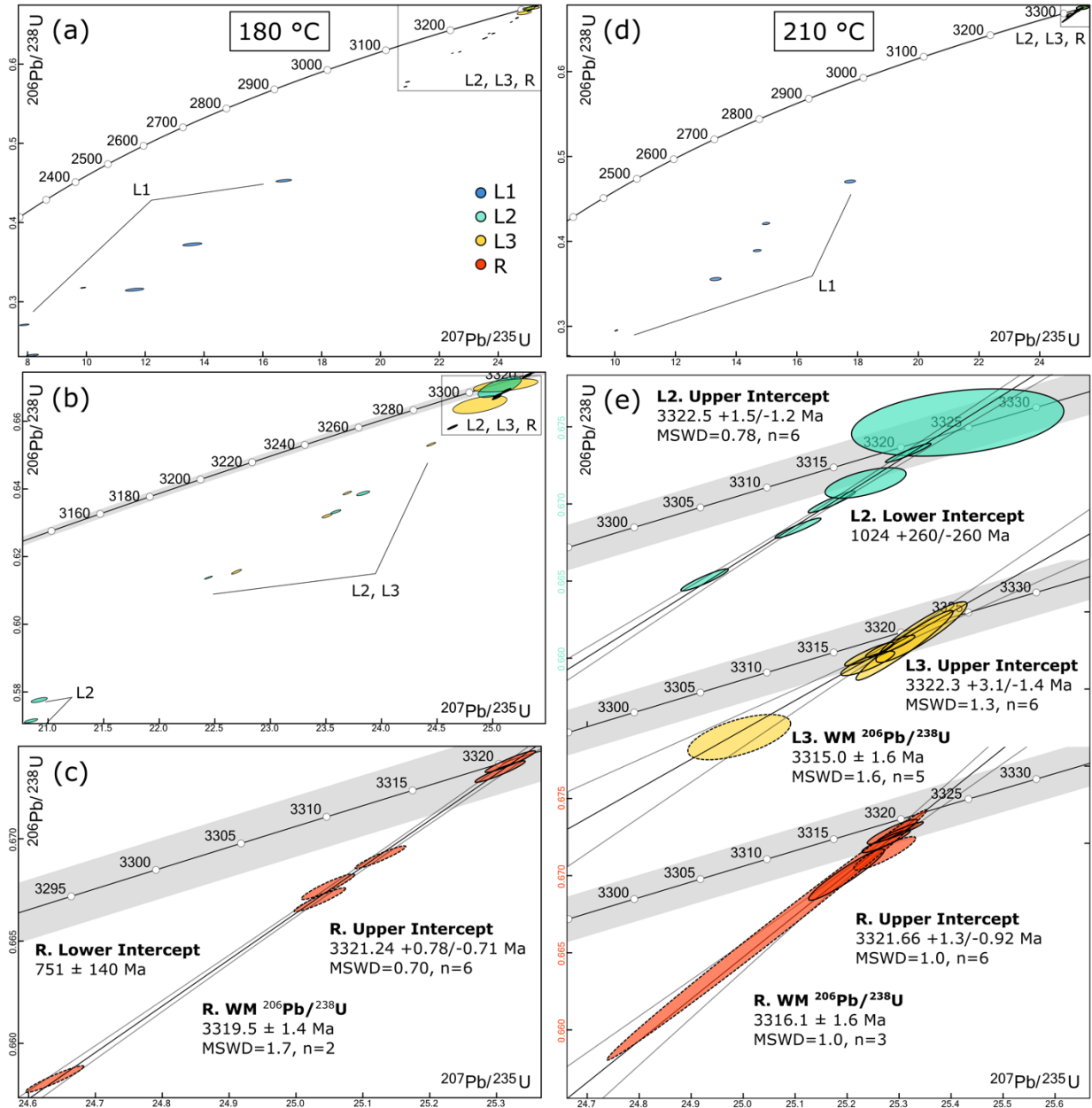
Figure 3. U-Pb concordia diagrams for the SAM-47 180 °C (left) and 210 °C (right) step-leaching experiments. **(a)** All data for the 180°C experiment. **(b)** Close up of the L2, L3, and R 180 °C dataset. **(c)** Close up of the 180 °C residue data. WM stands for weighted mean. **(d)** All data for the 210°C experiment. **(e)** Stacked plot showing the L2, L3, and R 210 °C datasets. All ellipses reflect 2σ analytical uncertainties. Dashed ellipses are excluded from weighted mean calculations.

956
957
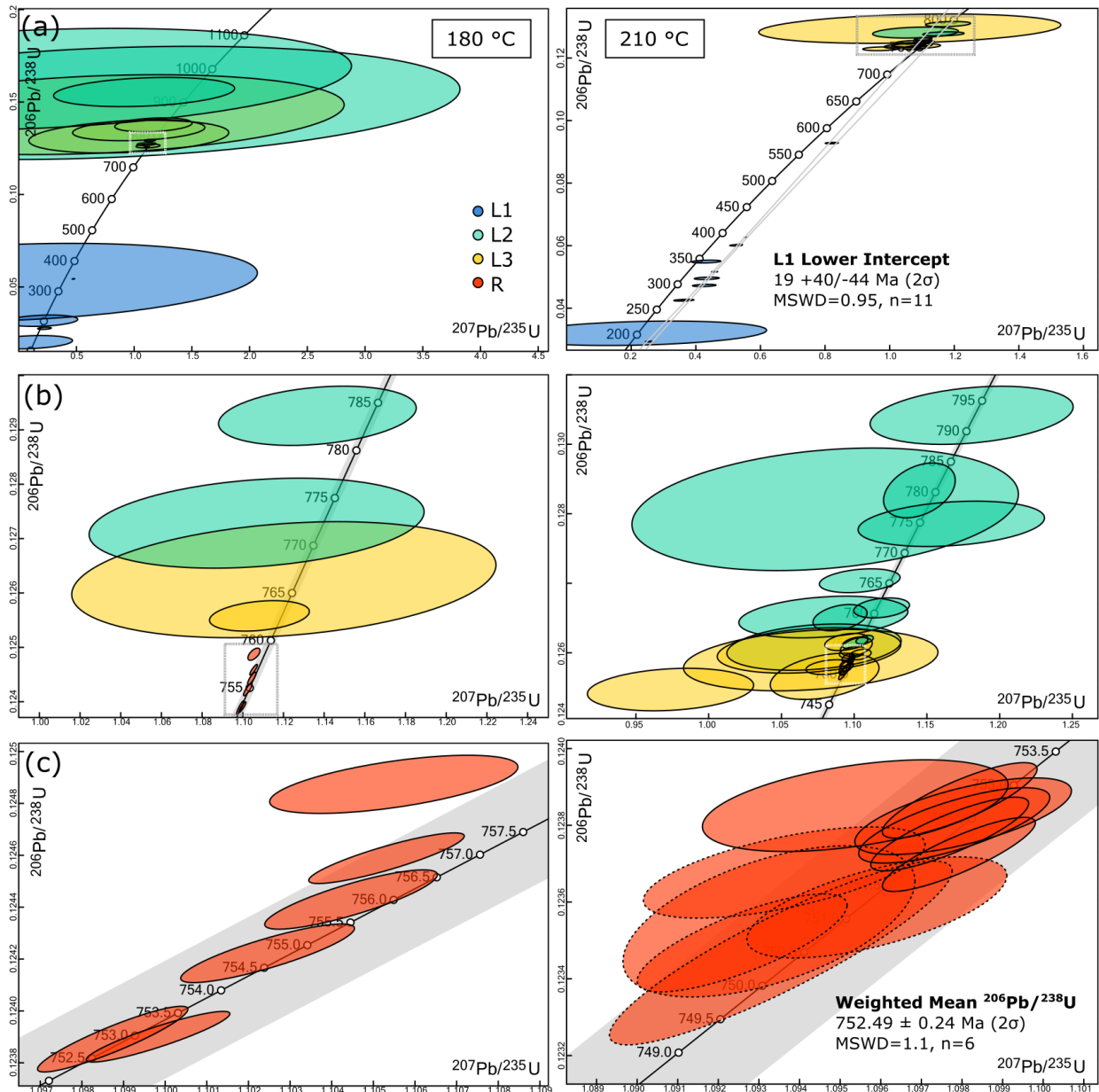
Figure 4. U-Pb concordia diagrams for the KR18-04 180 °C (left) and 210 °C (right) step-leaching experiments. **(a)** All data are depicted. **(b)** Close up of L2, L3, and R data excluding leachates with Pb*/Pb$_c$ values < 1. **(c)** Close up of zircon residues. The weighted mean ^{206}Pb/^{238}U date reported for the 210 °C experiment includes residue data with solid ellipse borders. Ellipses with dashed borders were excluded due to low-quality U measurements. All ellipses reflect 2σ analytical uncertainties.

958
959
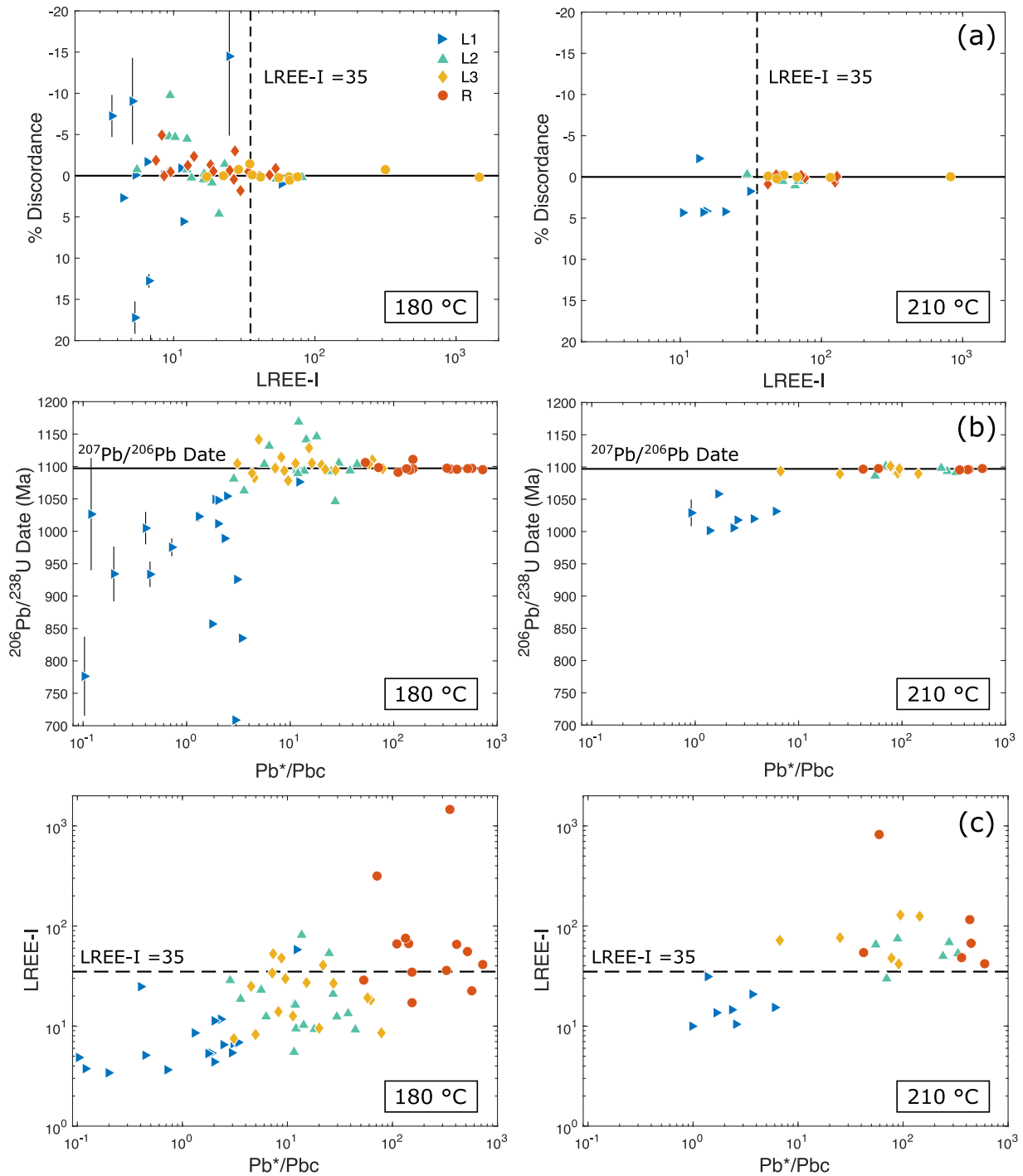
Figure 5. AS3 U-Pb and trace element data for the 180 °C (left) and 210 °C (right) experiments. **(a)** LREE-I versus percent discordance. The horizontal solid line represents perfect concordance. The vertical dashed line depicts a LREE-I threshold value of 35 below which data is notably more discordant. **(b)** ^{206}Pb/^{238}U date plotted as a function of the radiogenic Pb* to common Pb ratio. Error bars for the percent discordant and ^{206}Pb/^{238}U data reflect propagated 2σ analytical uncertainties. Most error bars are smaller than data markers. **(c)** The radiogenic Pb* to common Pb ratio versus the LREE-I showing a positive correlation between the two variables.

960
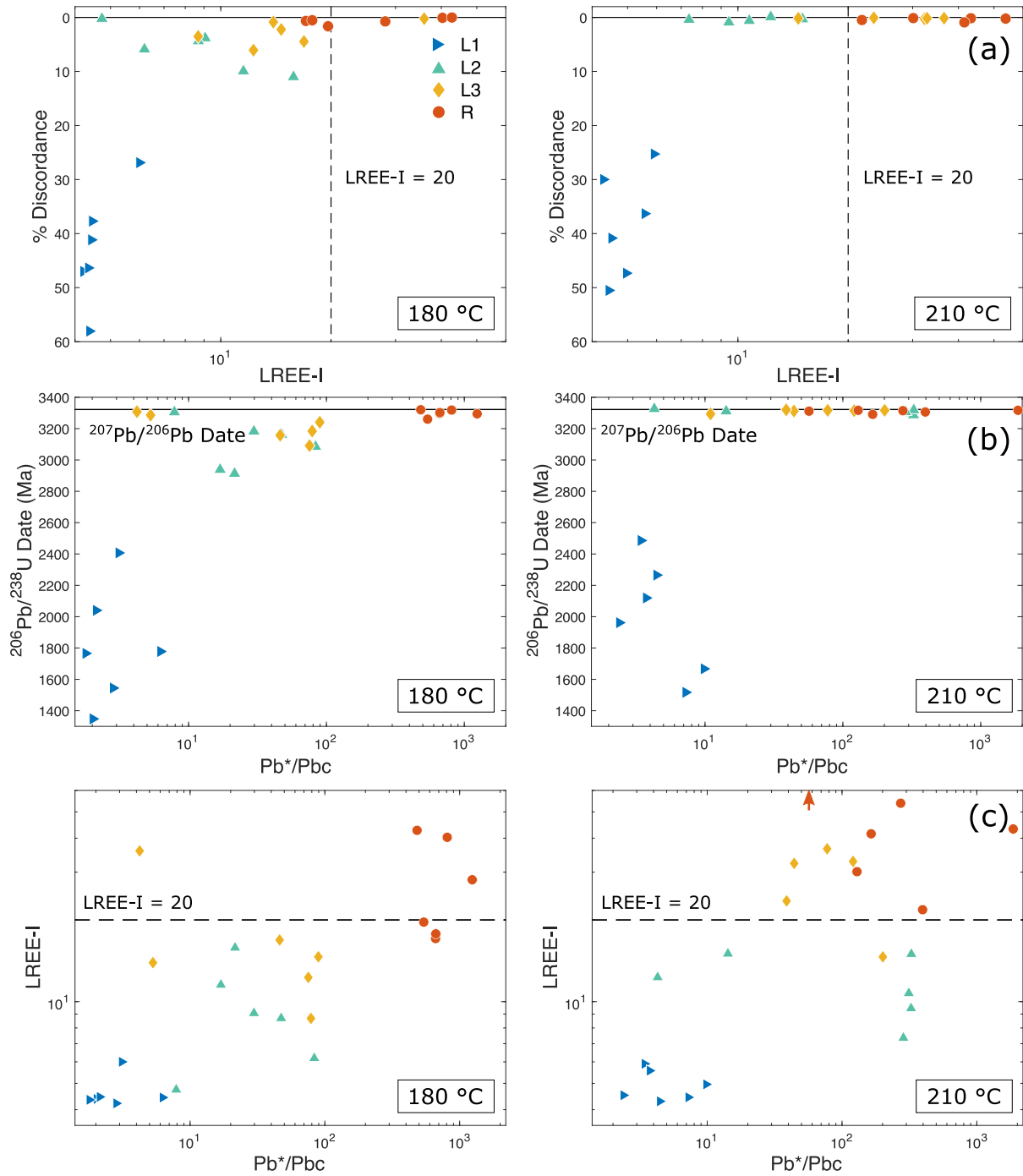
Figure 6. SAM-47 U-Pb and trace element data for the 180 °C (left) and 210 °C (right) experiments. **(a)** LREE-I versus percent discordance. The horizontal solid line represents perfect concordance. The vertical dashed line depicts a LREE-I threshold value of 20 below which data is notably more discordant. **(b)** ^{206}Pb/^{238}U date plotted as a function of the radiogenic Pb* to common Pb ratio. Error bars for the percent discordant and ^{206}Pb/^{238}U data reflect propagated 2σ analytical uncertainties. Most error bars are smaller than data markers. **(c)** The radiogenic Pb* to common Pb ratio versus the LREE-I showing a positive correlation between the two variables.

961
962
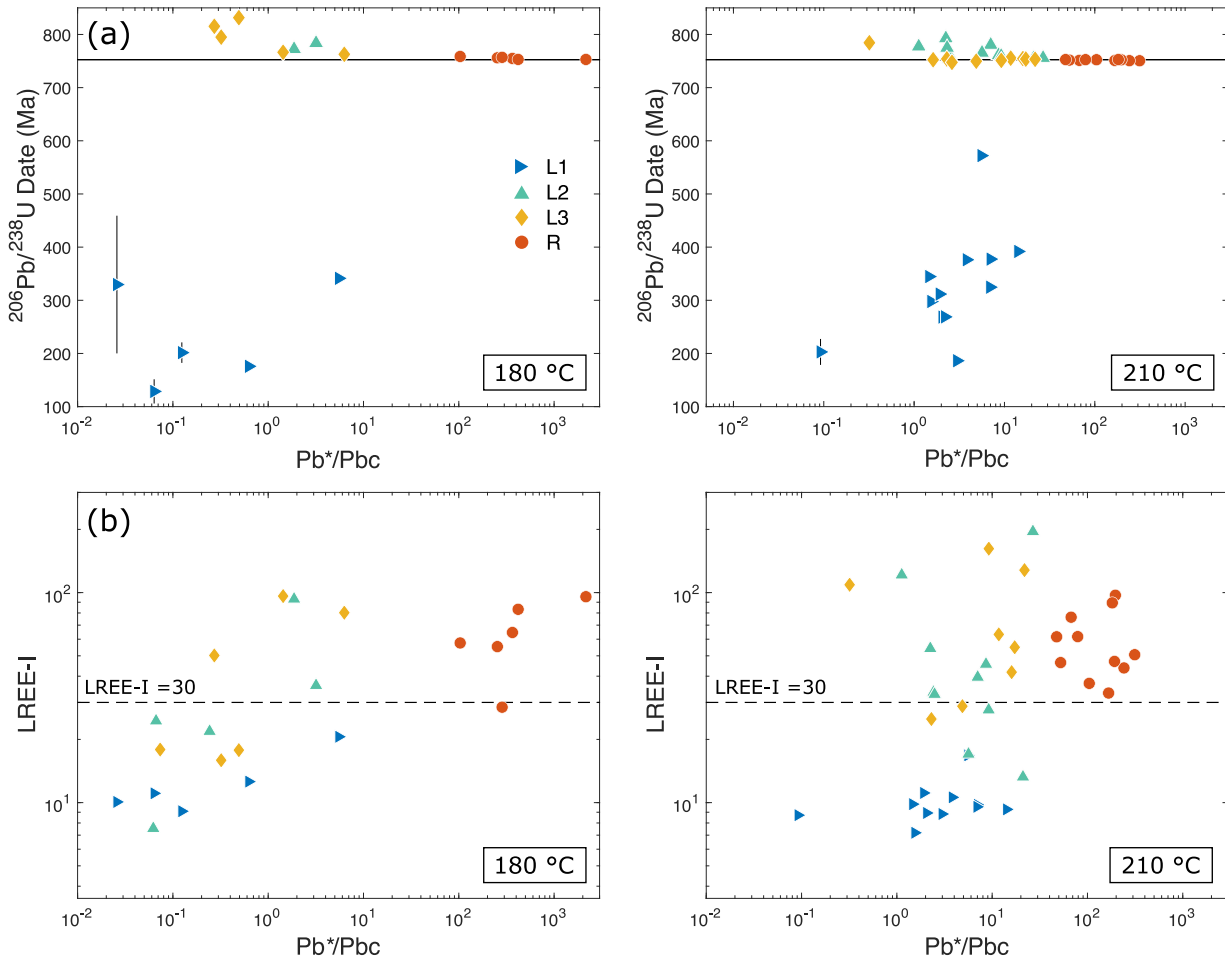
Figure 7. KR18-04 U-Pb and trace element data for the 180 °C (left) and 210 °C (right) experiments. **(a)** $^{206}Pb/^{238}U$ date plotted as a function of the radiogenic Pb* to common Pb ratio. 2σ analytical uncertainties for the percent discordant and $^{206}Pb/^{238}U$ data are smaller than data markers. **(b)** The radiogenic Pb* to common Pb ratio versus the LREE-I.

963
964
965
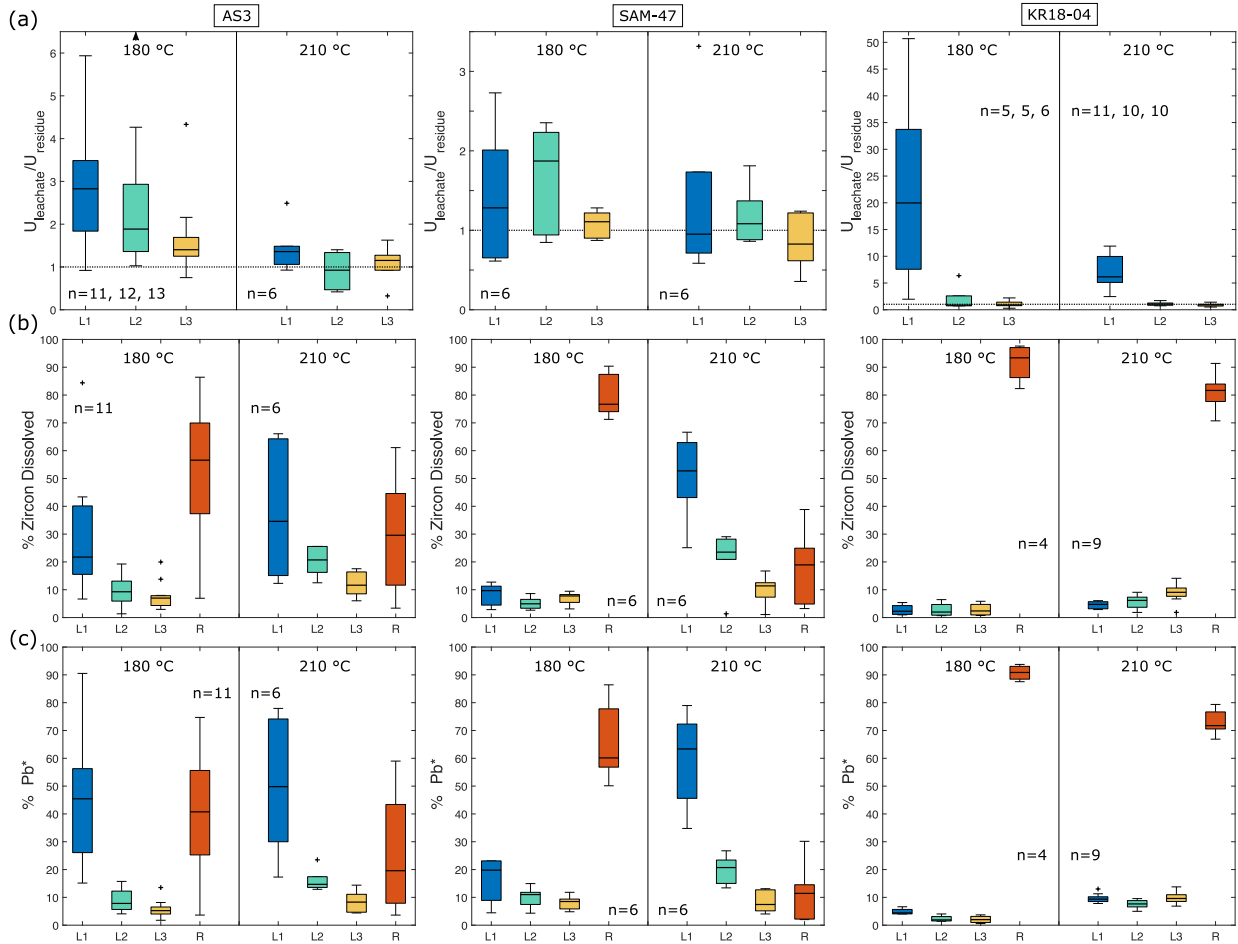
Figure 8. Box plot diagrams depicting geochemistry data for all step-leaching experiments. Each box shows the median value (black bar), the upper and lower quartiles (box), the minimum and maximum values (whiskers), and statistical outliers (plus marks) **(a)** Uranium concentration of leachates relative to that of their associated residue. **(b)** Percent zircon dissolved per leaching step based on measured Zr abundances. **(c)** Percent of radiogenic Pb measured per leaching step.

966
967
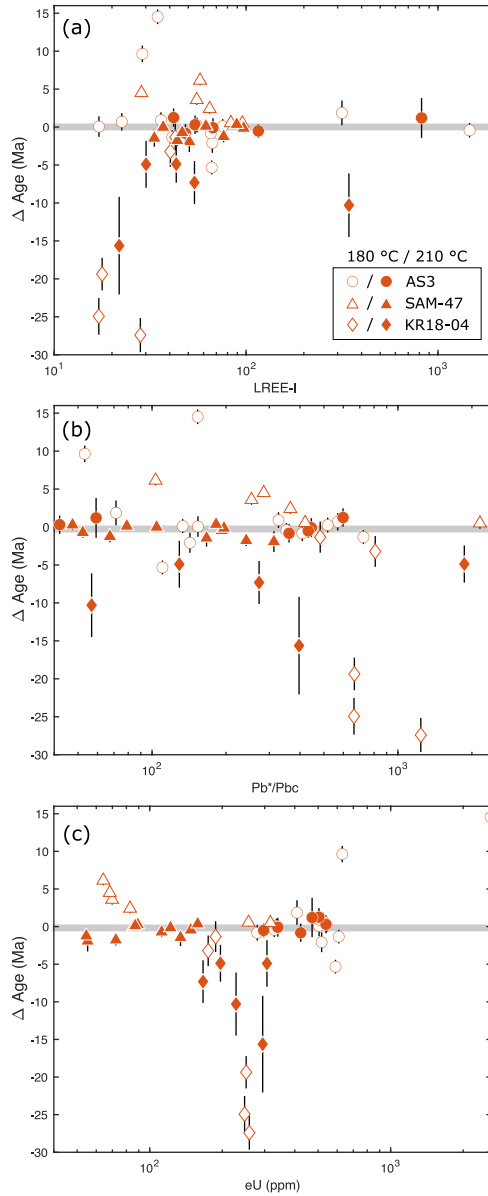
Figure 1. Trace element and Pb isotopic composition of zircon residues plotted against Δ Age as described in text. The gray bar at Δ Age = 0 Ma marks the accepted crystallization age for each zircon sample. **(a)** LREE-I versus the Δ Age. **(b)** Pb*/Pb$_c$ versus the Δ Age. **(c)** eU versus Δ Age. The arrow in each plot marks the placement of a datapoint from the SAM-47 dataset that plots at Δ Age = -60 Ma.

968
969
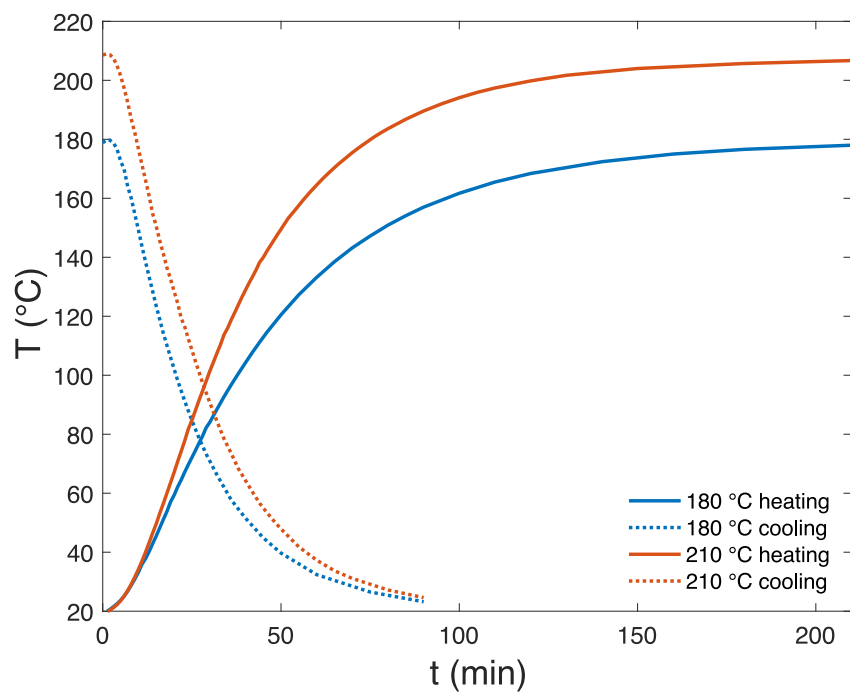
Figure 10. Temperature of the PTFE-lined pressure dissolution vessel plotted as a function of time. A fan was used to speed up cooling.

970
971
972
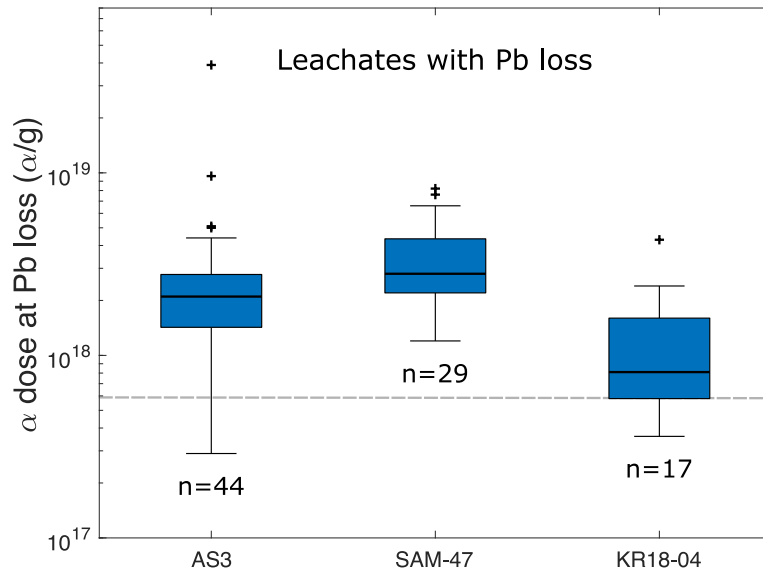
Figure 11. Box plot diagram showing alpha dose distribution for leachates (L1, L2, and L3) affected by Pb-loss. Data include both the 180 °C and 210 °C experiments. The gray dashed line highlights our best estimate for the minimum alpha dose required for Pb-loss to occur. Each box shows the median value (black bar), the upper and lower quartiles (box), the minimum and maximum values (whiskers), and statistical outliers (plus marks).

973
974
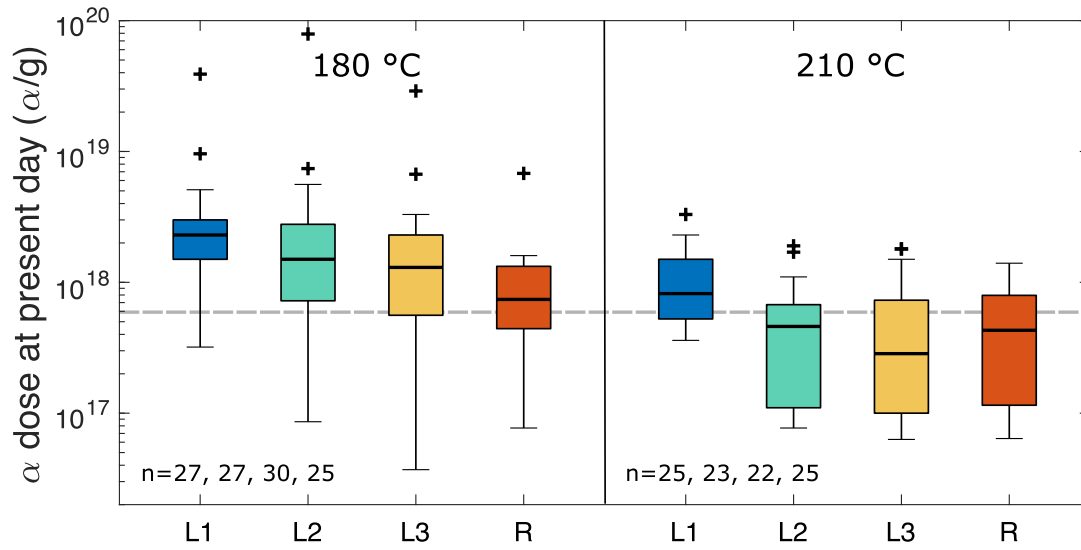
Figure 12. Box plot diagram showing present day alpha dose distributions at each step of zircon dissolution. Data includes all AS3, SAM-47 and KR18-04 leachates and residues. Alpha dose estimates reflect samples' present day radiation damage. The gray dashed line highlights our best estimate for the minimum alpha dose required for Pb-loss to occur. Each box shows the median value (black bar), the upper and lower quartiles (box), the minimum and maximum values (whiskers), and statistical outliers (plus marks).

975
976
977
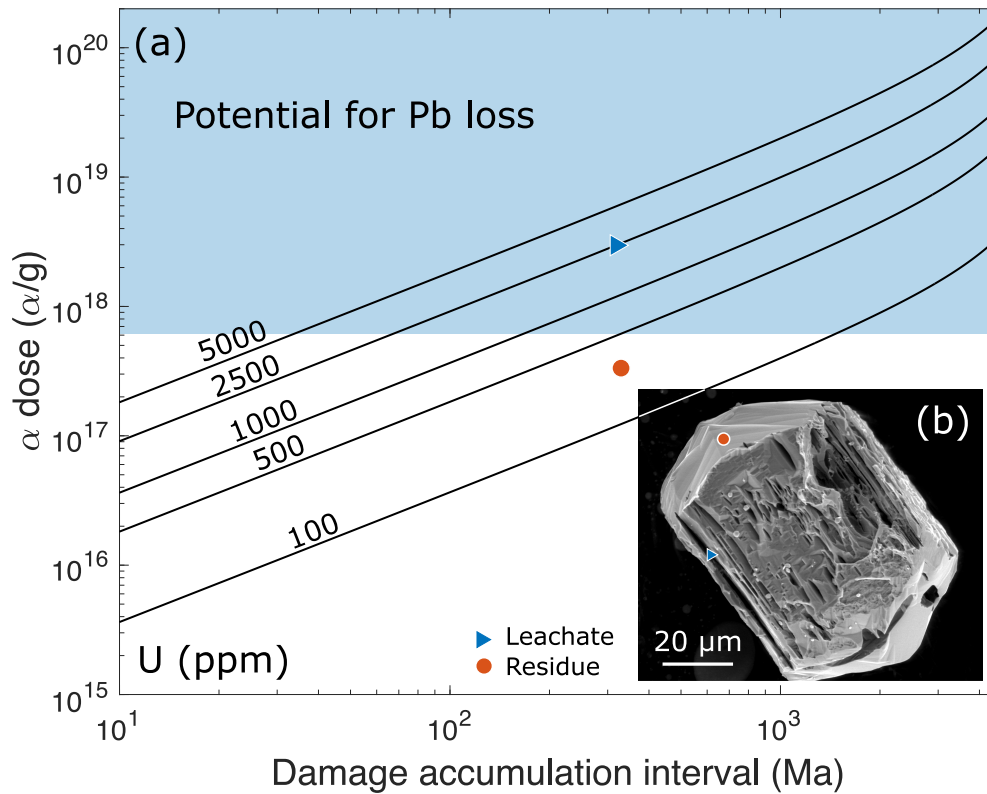
Figure 13. **(a)** Contour diagram showing alpha dose as a function of time for U concentrations ranging from 100 ppm to 5000 ppm. Calculations assume a fixed Th/U of 0.5 and no annealing. The shaded region highlights the alpha dose range in which Pb loss is most likely. **(b)** Secondary electron image of KR18-04 residue chemically abraded at 210 °C for 12 h from McKanna et al., (2023). The blue triangle marks a thin concentric zone that dissolved during chemical abrasion (leachate), while the red circle marks a portion of the zircon that remained intact (residue). Markers in b) correlate to markers in a) and illustrate how a grain with radionuclide zoning can have accumulated alpha doses above and below the threshold for Pb mobilization.

978
979
980

Table 1. Alpha dose estimates.

Sample	α dose (α/g)[1]						α_r dose (α/g)[2]	
	Total		Pb-Loss		Present Day		Present Day	
	Min	Max	Min	Max	Min	Max	Min	Max
AS3	4×10^{17}	1×10^{20}	3×10^{17}	8×10^{19}	3×10^{17}	8×10^{19}	2×10^{17}	$>1\times10^{19}$
SAM-47	2×10^{18}	1×10^{19}	1×10^{18}	8×10^{18}	3×10^{17}	2×10^{18}	6×10^{17}	2×10^{18}
KR18-04	1×10^{17}	1×10^{19}	4×10^{16}	4×10^{18}	4×10^{16}	4×10^{18}	5×10^{16}	7×10^{17}

[1]Calculated using measured U and Th concentrations and damage accumulation intervals as described in text.

[2]Raman-based alpha dose estimates reported by McKanna et al., (2023).

981